Fabrication of ZnO Scaffolded CdS Nanostructured Photoanode with Enhanced Photoelectrochemical Water Splitting Activity under Visible Light

Avinash Rokade[a], Ganesh K. Rahane[b], Aleksandar Živković[c], Swati N. Rahane[a], Hemant S. Tarkas[a], K. Hareesh[d], Nora H. de Leeuw[c,e], Shrikrishna Dattatraya Sartale[a], Nelson Y. Dzade[f], Sandesh R. Jadkar[a]*, Sachin R. Rondiya[b]**

[a]Department of Physics, Savitribai Phule Pune University, Pune 411007, India

[b]Department of Materials Engineering, Indian Institute of Science, Bangalore 560012, India

[c]Department of Earth Sciences, Utrecht University, Princetonlaan 8a, 3548CB Utrecht, The Netherlands

[d]Department of Physics, Manipal Institute of Technology Bengaluru, Manipal Academy of Higher Education, Manipal 576104, India

[e]School of Chemistry, University of Leeds, Leeds LS2 9JT, United Kingdom

[f]Department of Energy and Mineral Engineering, Pennsylvania State University, University Park, Pennsylvania 16802, United States

*Avinash Rokade - Email: avrokade88@gmail.com

*Sandesh R. Jadkar - Email: sandesh@physics.unipune.ac.in

*Sachin R. Rondiya - Email: rondiya@iisc.ac.in

KEYWORDS: ZnO/CdS, Nanostructures, Electrodeposition, Photoelectrochemical water splitting

ABSTRACT: CdS, characterized by its comparatively narrow energy bandgap (~2.4 eV), is an appropriate material for prospective use as a photoanode in photoelectrochemical water splitting. Regrettably, it encounters several obstacles for practical and large-scale applications, including issues like bulk carrier recombination and diminished conductivity. Here, we have tried to address these challenges by fabrication of a novel photoelectrode (ZnO/CdS) comprised of one-dimensional ZnO nanorods (NRs) decorated with two-dimensional CdS nanosheets (NSs). A facile two-step chemical method comprising of electrodeposition along with a chemical bath deposition was employed to synthesize the ZnO NRs, CdS NSs, and the ZnO/CdS nanostructures. The prepared nanostructures have been substantiated by UV-Visible absorption spectroscopy, X-ray diffraction, Raman spectroscopy, TEM, and scanning electron microscopy. The fabricated ZnO/CdS nanostructures have shown enhanced photoelectrochemical properties due to the improvement of the semiconductor junction surface area and visible light absorption. The incorporation of CdS NSs has been further found to promote the rate of charge separation and transfer process. Subsequently, the fabricated ZnO/CdS photoelectrodes achieved photocurrent conversion efficiency three times higher than that of a planar ZnO NRs photoanode and showed excellent performance under visible light irradiation. The highest applied bias photon-to-current conversion efficiency (% ABPE) of about ~ 0.63 % has been obtained for sample with thicker CdS NSs on ZnO NRs with photocurrent density ~ 1.87 mA/cm^2 under AM 1.5 G illumination. The newly synthesized nanostructures further demonstrates that the full photovoltaic capacity of nanomaterials is yet to be exhausted.

INTRODUCTION

The insufficient and limited supply along with the increasing pollution problems of existing conventional sources of energy, such a fossil fuels, have forced the world to start looking for clean, stable, and sustainable alternatives such as solar energy, hydrogen fuels, etc.[1] Solar energy is regarded as a highly promising renewable energy source that can substantially aid in the sustainable advancement of human society. For the effective harnessing of solar radiation, three primary challenges need to be tackled: the interception of sunlight, the transformation of sunlight into an appropriate and beneficial form of energy, and ultimately, the storage of this energy.[2] Furthermore, significant efforts are required to stabilize the inconsistent output of electricity derived from solar energy due to the daily and seasonal fluctuations of sunlight. Hydrogen has shown great promise as the future energy source. Water electrolysis is projected as a highly potential and environmentally friendly method for future hydrogen generation. The energy prerequisite for facilitating this hydrogen production can be harnessed from solar irradiation utilizing photoelectrochemical (PEC) cells. A PEC cell integrates both the energy capture and its conversion into hydrogen by splitting water in one inexpensive and efficient step.[3,4]

Significant global endeavors have been undertaken to investigate and improve various PEC systems,[5,6] including but not limited to TiO_2,[7] $SrTiO_3$,[8] $BaTiO_3$,[9] ZnO,[10] WO_3,[11] and α-Fe_2O_3[12]. However, due to their unfavorable electronic bandgaps, these proposed materials are incapable of absorbing a substantial portion of light in visible region. Conversely, several small energy bandgap materials like Si, GaAs, and GaP[13] have been scrutinized for PEC processes, but they have failed to generate the necessary photo potential and are prone to rapid corrosion upon contact with the electrolyte. Numerous modification strategies have been experimented on these semiconductors, including the addition of dopants,[14] co-doping,[15] sensitization by dye/quantum dots,[16] synthesis of

multilayered homo/hetero-structures,[17] surface engraving,[18] attachment of plasmonic noble metals,[19] irradiation with swift heavy ions,[20] etc., yet they have not yet achieved an efficient photoanode for the process of water splitting.

ZnO, identified as an n-type semiconductor, having a direct bandgap energy of 3.37 eV at room temperature and demonstrates a comparatively high carrier mobility that varies within a range 115-155 cm^2 $V^{-1}s^{-1}$.[21,22] Its properties make it a prospective contender for use in optoelectronic applications, specifically as emitters of ultraviolet light.[23,24,25,26,27] Due to the high bandgap value, intrinsic ZnO films do not absorb in the visible range, thus effectively missing to absorb the most abundant number of photons from the UV spectrum and making ZnO a poor choice for practical applications. One-dimensional nanostructures are gaining recognition as potential alternatives to planar thin films, owing to their optimal geometric arrangements that provide a straightforward pathway for charge transport and a significant surface area at the junction. Compared with ZnO thin films, 1D nanostructured ZnO nanorods (NRs) base layers offer the advantages of potentially higher accessible surface areas, address short charge diffusion, and a bridge for rapid carrier transport[28,29,30,31,15] The nanosheet-nanorod coupled nanostructures have various benefits over the thin film semiconductor junctions like a substantially more surface area leading to increased interaction of photons with the material there by reducing the electron-hole recombination losses, rapid charge separation and transfer processes. Beyond the alteration of morphology and structure, ZnO NRs can be integrated with small bandgap substances like CdS, CdSe, PbS, or Fe_2O_3.[32] CdS, being one of the most frequently used semiconductor sensitizers, stands out due to its narrow bandgap (2.4 eV) and a conduction band edge that is situated above that of ZnO. The type-II bandgap arrangement of the ZnO/CdS nanostructures enables the transfer of excited electrons from CdS to ZnO.[33] This separation of electrons and holes leads to a substantial extension in the exciton

lifetime and a decrease in the recombination rate of photogenerated electron-hole pairs, thereby enhancing PEC water splitting for hydrogen production. In the type-II arrangement, the conduction band minima of CdS and ZnO are positioned at -4.1 eV and -4.3 eV with respect to vacuum, respectively. Thus, here an attempt has been made to photosensitize ZnO NRs with the addition semiconducting CdS nanosheets (NSs) as a visible active layer. The fabricated hierarchical ZnO/CdS nanostructures morphologies exhibit a significant performance upon visible light irradiation.

In the existing literature, there is a gap in the preparation of CdS/ZnO nanostructures that are anticipated to exhibit effective separation of photogenerated charge-carrier pairs, thereby inhibiting their recombination. Inspired by this, we have engineered ZnO NRs sensitized with CdS NSs to form ZnO-NRs/CdS nanostructures using a simple two-step synthesis procedure, namely electrodeposition and chemical bath deposition techniques. An extensive investigation has been conducted using x-ray diffraction (XRD), Raman spectroscopy, UV-Visible spectroscopy, scanning electron microscopy (SEM), energy dispersive X-ray (EDX) spectroscopy, transmission electron microscopy (TEM), electrochemical impedance spectroscopy (EIS), Mott-Schottky analysis, and applied bias photon-to-current conversion efficiency (% ABPE) measurements.

EXPERIMENTAL DETAILS

Chemicals

Zinc Nitrate ($Zn(NO_3)_2$), Hexamethylenetetramine (HMT), Cadmium Sulphate ($CdSO_4$), Thiourea (CH_4N_2S), and Ammonium Hydroxide (NH_4OH). Chemical reagents of AR grade (99.99% pure) were employed without any additional purification for all the experiments.

Synthesis of ZnO NRs, CdS NSs and ZnO/CdS nanostructures

ZnO NRs were fabricated on a conductive fluorine-doped tin oxide (FTO) substrate utilizing a straightforward, economical, and eco-friendly electrodeposition technique. The working, counter, and reference electrodes were constituted from the FTO substrate, Pt foil, and saturated calomel electrode (SCE), respectively. Electrochemical studies were conducted using an Autolab potentiostat N32 model, managed by a personal computer, in a tri-electrode cell arrangement equipped with NOVA 1.11 electrochemistry software.

A fundamental requirement for the electrodeposition technique is the conductivity of the substrate, which is essential for establishing a complete electrolytic circuit. In this investigation, we employed a conducting FTO substrate measuring 2cm x 1cm, characterized by a sheet resistance of approximately 15 Ω/cm² and a thickness in the range of 150-200 nm. Prior to initiating the deposition, substrates underwent a cleaning process in an ultrasonic bath utilizing detergent, acetone, ethanol, and DDW for a duration of 5 mins each. Post-cleaning, the substrates were subjected to drying using a flux of dry air.

The preparation of ZnO NRs thin films was executed via electrochemical deposition (Figure 1). Initially, around 0.28 M of zinc nitrate and 4.9×10^{-2} M of HMT were mixed in 100 mL of DDW. This concoction was agitated for approximately 30 mins until the pH attained 6.2. Once the solution was thoroughly mixed, 0.28 M of NaOH was gradually put in to increase the basicity of solution, leading to pH of 12.4. A white suspension briefly formed in the beaker before returning to its original state. Subsequently, the solution was relocated to a 250 mL glass container and subjected to a temperature of 80 °C for a duration of two hours.

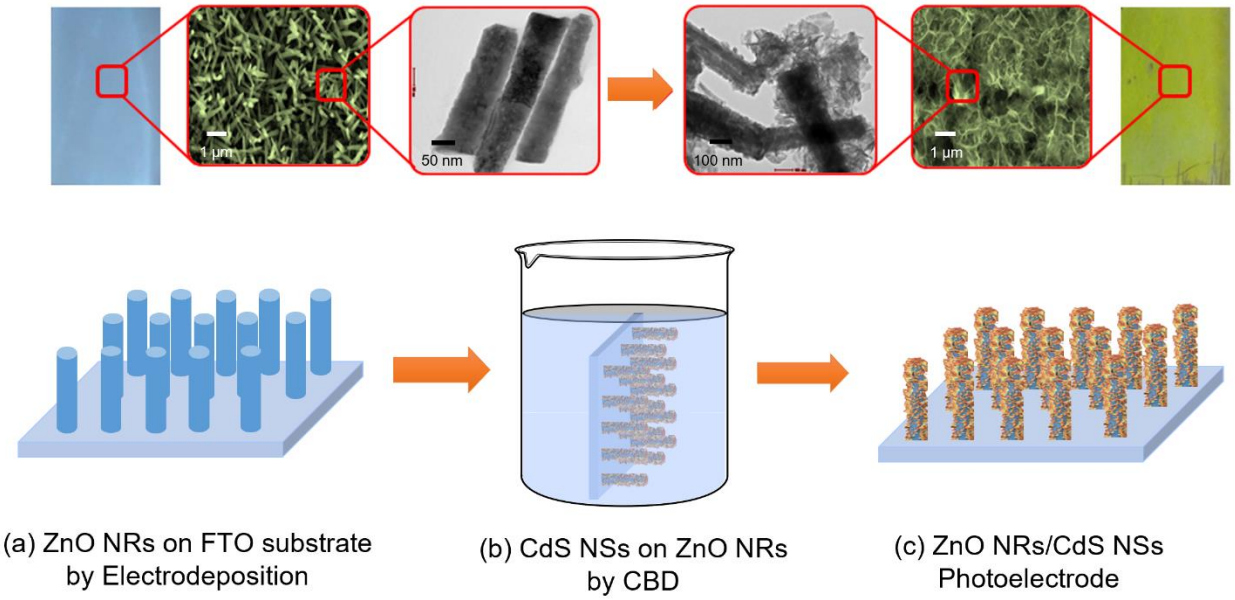

Figure 1. Graphic explaining the preparation of (a) of ZnO NRs, (b) CdS NS on ZnO NRS (5, 10, 20, 30 mins) and (c) Prepared CdS NSs on ZnO NRS nanostructures.

Initially, no changes were observed, but as the temperature increased, the initial formation of NRs began. Throughout this process, a steady potential of approximately -0.85 V was maintained for a period of 2 hours to facilitate the growth of adequately dense NRs on the surface of the FTO substrate.

The Chemical Bath Deposition (CBD) technique was employed to fabricate the CdS NSs thin films on both the FTO substrate and on top of ZnO NRs (Figure 1). The synthesis of CdS NSs was carried out in an aqueous medium (DDW, 350 mL) with specifically optimized molarities of cadmium sulphate ($CdSO_4$, 3 mM), thiourea (CH_4N_2S, 2.4 mM), and ammonium hydroxide (NH_4OH, 4.4 M (40 mL)) to keep pH of a solution at 11. The ZnO/CdS heterostructures were synthesized by immersing FTO glass substrate and ZnO NRs films in a solution maintained at 70 °C. This immersion was performed for distinct time intervals (5, 10, 20, and 30 mins) to prepare

the required thickness of CdS NSs on the ZnO NRs films. Post-deposition, the fabricated films underwent a thorough rinse in DDW and were dried up below a compressed air gun. This was succeeded by an annealing process at 400 °C for a duration of 1 hour to eliminate moisture and rectify defects inherent in the samples.

Characterization of ZnO NRs, CdS NSs, and ZnO/CdS heterostructures

The surface texture of the films was examined using a JEOL JSM-6360A scanning electron microscope (SEM) operating at a voltage of 20 kV. X-ray Diffraction (XRD) patterns were procured using an X-ray Diffractometer (Bruker D8 Advance, Germany) with a Cu-K_α line (λ = 1.54 Å). The optical bandgap of the thin films was inferred from absorption measurements conducted using a JASCO, V-670 UV-Visible spectrophotometer within the range of (200-800) nm. Raman spectra were captured using Raman spectroscopy (Jobin Yvon Horibra LABRAM-HR) within the range (150-900) cm^{-1}, utilizing a 632.8 nm line of a He-Ne laser as the excitation. The Raman laser power was maintained below 5 mW to prevent crystallization on the films due incident laser light. Further investigation into the surface texture and crystalline characteristics of the synthesized films was conducted using Transmission electron microscopy (TEM, Tecnai G2 20 Twin, FEI). The ZnO NRs, CdS NSs, and ZnO/CdS nanostructures were scraped off from the substrate surface and the resulting powder was dispersed ultrasonically in ethanol for a duration of 5 mins, to perform TEM investigation, moreover, for TEM analysis, a droplet of ultrasonicated solution was deposited on the carbon-coated copper grid.

PEC water splitting

The prepared ZnO NRs, CdS NSs, and ZnO/CdS nanostructures photoanodes were employed as working electrodes (WE) for PEC measurements. The other electrodes used for the measurements

are Pt foil (as counter electrode) and saturated calomel electrode (as reference electrode), which were placed inside the cell containing 0.5 M Na_2SO_4 electrolyte. Metrohm Autolab PGSTAT302N Potentiostat and a 150 W Xenon Arc Lamp (PEC-L01), with a light intensity of 100 mW/cm^2 (AM 1.5), were used to investigate the current-voltage (I-V) properties. The same potentiostat (Model: FRA 32M) was used to perform EIS measurements. The photo EIS measurements were carried out in a 0.5 M Na_2SO_4 electrolyte at 0.5 V, with the frequency kept within the range of 0.1 Hz to 100 kHz. In the absence of light, the Mott-Schottky (MS) plot of the ZnO-NRs samples ($1/C^2$ vs. electrode potential) was documented at a frequency of 500 Hz to ascertain the flat band potential (V_{fb}), donor density (N_d), and the width of the space charge layer (w).[34,35,36]

Computational details

Calculations based on the spin-polarized density functional theory (DFT) were conducted utilizing the Vienna ab-initio simulation package (VASP v5.4.4).[37–39] This was executed in harmony with the projector-augmented wave (PAW) methodology, incorporating a plane-wave energy limit of 450 eV. The valence electronic configurations designated for the PAW potentials encompassed $5s^2 4d^{10}$ for Cd, $4s^2 3d^{10}$ for Zn, $2s^2 2p^4$ for O, and $3s^2 3p^4$ for S. The presented calculations employed the PBE0 global hybrid DFT functional.[40,41]

Structural optimizations were performed using the conjugate gradient technique, with the convergence criteria for total energy and force established at 10^{-6} eV and 0.01 eV/Å, respectively. The Brillouin zone underwent sampling with a Γ-centred Monkhorst-Pack mesh of dimensions 7x7x5 and 5x5x5 for the bulk ZnO and CdS, respectively.[42] Appropriate band paths, in line with the symmetry of the crystal space group, were classified using the SeeK-path method.[43,44] The electron and hole effective masses were calculated using Sumo.[45] Visual representations were

generated utilizing the VESTA software.[46] The electronic band structure, computed utilizing PBE0 within the framework of the PAW formalism, was interpolated based on Wannier functions employing the Wannier90 code (v3.1.0).[47–49]

The METADISE[50] code was utilized to generate the non-polar surfaces of ZnO and CdS. These surfaces were represented as a slab of materials with periodic boundary conditions in the planar orientation and a vacuum layer perpendicular to the surface. A vacuum region of at least 15 Å was deemed sufficient to inhibit interactions between the periodic slabs. For the characterization of the surface, the surface energy (γ), acting as a measure of thermodynamic stability, was computed using the following formula:

$$\gamma = \frac{E(n) - n \cdot E_{bulk}}{2 \cdot A} \quad (1)$$

where, $E(n)$ represents the energy associated with a slab composed of n-layers, E_{bulk} denotes the energy intrinsic to the bulk material, and A signifies the area of the surface under consideration. The vertical ionization potential (IP) is calculated using a bulk-based definition, via the electrostatic alignment between the surface and the bulk as follows:[51,52]

$$\varepsilon_{IP} = \Delta\varepsilon_{\text{vac-ref}} - \Delta\varepsilon_{\text{VBM-ref}} \quad (2)$$

where $\Delta\varepsilon_{\text{vac-ref}}$ is the change among the electrostatic potential in the vacuum region[53,54] and the slab's bulk-like reference level (the 1s states of Cd and Zn situated in the center of the CdS (111) and ZnO (100) slabs, respectively) is considered. The second term, $\Delta\varepsilon_{\text{VBM-ref}}$, represents the discrepancy in eigenvalue energy between the valence band maximum (VBM) and the reference level derived from bulk computations. The electron affinity (EA) is ascertained by deducting the obtained bandgap value from the ionization potential. Calculations of lattice dynamics were performed using a supercell method within the harmonic approximation, utilizing the all-electron

(AE) code CRYSTAL (2017 release) with the hybrid PBE0 exchange-correlation functional.[55–58,40,41] The Gaussian basis sets used were taken unaltered from the CRYSTAL library: triple-ζ-valence + polarization (pob-TVZP) for Zn,[24,55] TZVP for O optimized by Linnera *et al.*,[56,57], an effective core pseudopotential for Cd by Heyd *et al.,* [58] and pob-TZVP for S from Peintinger *et al.*[44]. Within CRYSTAL, the convergence of the real-space summation of the Coulomb and exchange components to the Hamiltonian matrix is governed by five intersecting conditions. The quantities employed in this investigation were 10^{-7}, 10^{-7}, 10^{-7}, 10^{-9}, and 10^{-30}. The sample employed for the initial Brillouin zone for the bulk of ZnO and CdS are Monkhorst-Pack grids of dimensions 9x9x7 and 7x7x7, respectively.[59]

RESULTS AND DISCUSSION

X-ray Diffraction analysis

The structural properties of ZnO NRs, CdS NSs, and ZnO/CdS heterostructures have been characterized using XRD and are shown in Figure 2a. The XRD patterns were all procured at a grazing incidence angle of 1^0, with a step increment of 0.5^0, utilizing a continuous scan mode. The XRD pattern of the ZnO film exhibited prominent diffraction peaks at 2θ values approximately equal to 31.70^0, 34.40^0, 36.20^0, 47.50^0, and 56.50^0. These peaks correspond to the (100), (002), (101), (102), and (110) planes of the hexagonal wurtzite structure of ZnO, which is consistent with the JCPDS #80-0075. These findings substantiate the creation of highly crystalline ZnO films, exhibiting a favored orientation along the (002) plane direction. No impurities peaks were found except the diffraction peaks of FTO substrate. The peaks marked with a star (*) belong to the FTO substrate used. The peaks at $2\theta \sim 31.7^0$(100), 34.4^0(002), 36.2^0(101), 47.5^0 (102), and 56.5^0 (110) corresponding to hexagonal wurtzite of ZnO NRs. Major diffraction peak at $2\theta \sim 36.5^0$ corresponds

to the (111) plane characteristic of the CdS cubic structure. The evaluation of interplanar spacing (d-spacing) predicated on a hexagonal lattice structure can be conducted utilizing,

$$\frac{1}{d^2} = \frac{4}{3}\frac{h^2+hk+k^2}{a^2} + \frac{l^2}{c^2} \quad (3)$$

where h, k, and l represent the Miller indices, and a and c denote the lattice constants. The values for the interplanar spacings (d) were determined to be d_{100}=2.82 Å, d_{002} =2.60 Å, and d_{101}=2.48 Å. The lattice parameters, a and c, were found to be 3.25 Å and 5.21 Å, respectively. These values align with the typical lattice parameters for the hexagonal ZnO phase (JCPDS #36-1451 for ZnO, d_{100}=2.8143 Å, d_{002} =2.6033 Å, d_{101}=2.4759 Å, a=3.249 Å c=5.206 Å).[60,61] The XRD pattern of CdS film is shown in Figure 2a which depicts diffraction peak at 2θ ~ 26.50° corresponding to the (111) plane which is in agreement with JCPDS #75-1531.

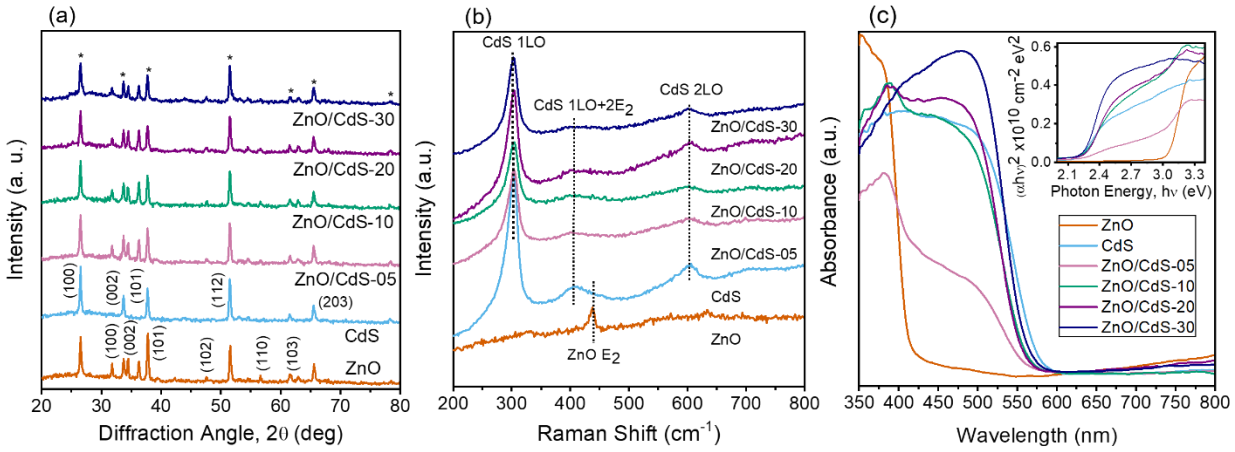

Figure 2. (a) X-ray diffraction pattern of i) ZnO NRs, ii) CdS NS, and ZnO/CdS hetero-structures prepared at different dipping durations iii) 5 mins, iv) 10 mins, v) 20 mins, and vi) 30 mins. The peaks marked with star (*) belong to the underlying FTO substrate used. (b) Raman spectra of i) ZnO, ii) CdS, and ZnO/CdS hetero-structures prepared at different dipping durations iii) 5 mins, iv) 10 mins, v) 20 mins, and vi) 30 mins. (c) UV-Visible absorptance spectra of the ZnO-NRs, CdS-NSs and ZnO/CdS hetero-structures

prepared at various dipping durations, inset shows the Tauc plot used for the measurement of the bandgap energy.

Figure 2a shows the XRD pattern of ZnO/CdS heterostructure films, depicting the peaks corresponding to those of ZnO NRs with a characteristic wurtzite structure, the CdS NSs with a characteristic cubic structure and FTO substrate. These results confirmed the formation of ZnO/CdS nanostructures.

Raman spectroscopy analysis

The confirmation about formation of ZnO NRs, CdS NSs, and ZnO/CdS nanostructures has been corroborated by Raman spectroscopy, as depicted in Figure 2b. The most compelling proof of the formation of the Wurtzite ZnO structure is derived from the analysis conducted via Raman spectroscopy. Figure 2b illustrates a pronounced Raman peak, centered approximately at 437 cm^{-1}. This peak is indicative of the E_2 high-frequency mode of ZnO, primarily involving the motion of Zn atoms, and is characteristic of the Wurtzite phase.[60] For CdS sample, we observed three major optical vibrational Raman active modes approximately around 302, 390, and 603 cm^{-1}. The strong and wide-ranging spectral peaks that emerged around 302 and 600 cm^{-1} were attributed to the fundamental optical phonon mode (LO), and the first overtone mode (2LO) of CdS, respectively. The existence of hexagonal Wurtzite CdS was further corroborated by the detection of two Raman shoulders positioned approximately at 302 cm^{-1} and the weak peak positioned around ~600 cm^{-1}.[62] The Raman spectra for the ZnO/CdS sample exhibit three distinct peaks, approximately at 437, 302, and 600 cm^{-1}, which correspond to the longitudinal optical (LO) vibrational modes of ZnO and CdS, thereby affirming the successful formation of a ZnO/CdS nanostructures. It is noteworthy that in the ZnO/CdS nanostructures, CdS has demonstrated a

reduction in Raman scattering relative to ZnO, which could be attributed to the absorption of photons by the CdS layers.

UV-Visible spectroscopy analysis

Figure 2c represents the UV-Visible optical absorption spectra that were employed to determine the bandgap of both ZnO NRs and ZnO/CdS nanostructures. The absorption spectra of the ZnO and ZnO/CdS core-shell nanostructures facilitate the approximation of the absorption edges by extending the curves to the energy axis, where the zeroes roughly align with the bandgap energies. Figure 2c presents absorption spectra of the ZnO NRs, CdS NSs, and ZnO/CdS nanostructures fabricated at different dipping durations. The absorption spectra reveals that the ZnO-NRs primarily absorb in the UV region, with the absorption edge situated approximately at (400-410) nm. An increase in the CdS-NSs loading on ZnO-NRs, the absorption edge can be drastically extended from around ~ 400 nm for ZnO to ~ 570 nm for ZnO/CdS, which is closer to the one of pure CdS. With the increment in CdS loading duration, both the particle size and the quantity of CdS progressively amplified, thereby inducing a redshift in absorption because of the size quantization effect.[63] Consequently, the bandgap energy experiences a substantial reduction from 3.2 eV to 2.2 eV. The inset of Figure 2c depicts the characteristic Tauc's plot employed for the estimation of the bandgap energy. Thus, loading CdS-NSs on ZnO-NRs can enhance visible light absorption and subsequently improve the PEC response. The deduced bandgap values for ZnO and the ZnO/CdS nanostructures are 3.2 eV and 2.4 eV, respectively. These quantifications substantiate the existence of both the CdS and ZnO phases within the film. The bandgap values procured align well with previous reports.[64]

Scanning electron microscopy analysis

The surface texture of ZnO, CdS, and ZnO/CdS nanostructures has been investigated by scanning electron microscopy. Figures 3a and 3b show SEM micrographs of ZnO and CdS thin films whereas Figures 3c-f shows SEM micrographs ZnO/CdS nanostructures prepared at 5-, 10-, 20-, and 30-mins dipping duration, respectively. As seen from Figure 3, all films are dense, homogenous, and free from defects and cracks. The Scanning Electron Microscopy (SEM) micrograph of the ZnO thin film, as depicted in Figure 3a, reveals a surface morphology characterized by uniform, dense, and highly crystalline formation of hexagonal NRs. The well-structured hexagonal ZnO NRs, with an average diameter in the range of approximately 150-200 nm and length of about 1-2 μm, are discernible in Figure 3a. Moreover, the picture indicates these self-controlled and vastly structured rods are oriented at a right angle to the substrate, entirely soft and close to unblemished along their length, and importantly, lack any undulations on their surfaces. The SEM image of the CdS film (Figure 3b) displays a sheet-like morphology with an average edge length of approximately 400-500 nm. These NSs tangle to each other forming the film and less defects such as pores or pinholes were observed on the surface or throughout the film. As seen from Figure 3c, ZnO-NRs are encapsulated by the thin layer of CdS-NSs, when ZnO/CdS heterostructures prepared for 5 mins dipping time only. However, as discernible from Figure 3c, the highly ordered texture is preserved even after the ZnO NRs are stacked with CdS NSs. The CdS-NSs are homogeneously distributed across the surface of the ZnO-NRs. A slender layer of CdS-NSs envelops the entire surface of the ZnO-NRs, thereby augmenting the total surface area available for absorption. Given that the proliferation of CdS is dictated by the reactive surface of ZnO following the encapsulation of the total surface area, the expansion of CdS on ZnO NRs is impeded. With a further extension in dipping duration, the reaction decelerates and ultimately ceases. These nanostructures are advantageous for the radial separation of photo-induced charge

carriers. Figure 3d illustrates that, with an increase in dipping duration, a mesh-like formation develops and envelops the entire surface of the ZnO NRs. As the dipping time is further extended, the mesh formation thickens to such an extent that the ZnO-NRs become barely discernible, as can be observed from the top view of the Scanning Electron Microscopy (SEM) micrographs (Figures 3e-f). The surface morphology of ZnO-NRs/CdS NSs is composed of aggregates of ZnO NRs and columnar CdS NSs grown in a direction normal to the layer surface. The matrix structure composed of NSs and NRs is advantageous for the radial segregation of photo-induced charge carriers.[35]

Energy dispersive X-ray spectroscopy analysis

The compositional characterization of the ZnO/CdS nanostructures was performed utilizing the EDX tool. A representative EDX spectrum, captured in the binding energy range of (0-10) KeV for the specimen subjected to a dipping duration of 30 mins during the CBD growth of CdS NSs on ZnO NRs to achieve optimum thickness (ZnO/CdS-30) hetero-structure, is depicted in Figure 3h. The inset of Figure 3h summarizes the analyzed chemical compositions of the prepared nanostructures, providing the atomic percentages of the constituent elements Zn, O, Cd, and S. Figure 4g shows the elemental mapping of chemical constituents present in ZnO/CdS-30 nanostructures obtained from SEM-EDX spectra. As seen from Figure 3i-l, the elemental mapping clearly reveals the even elemental distribution of Zn (red), O (orange), Cd (blue), and S (green) in the ZnO/CdS-30 nanostructures, respectively. The elemental composition of Zn, O, Cd, and S in ZnO/CdS-30 nanostructures identified from EDX spectra, and the observed composition shown in the inset of Figure 3h are in good agreement.

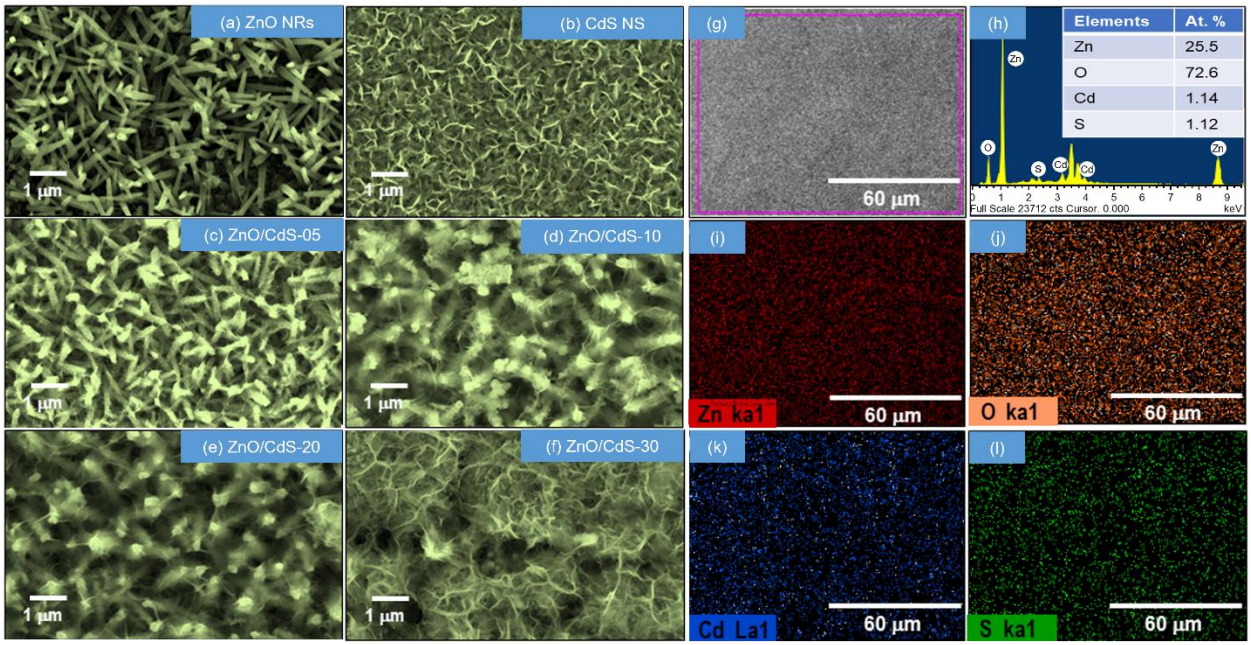

Figure 3. SEM pictures of (a) ZnO-NRs, (b) CdS-NSs, and ZnO-NRs/CdS-NSs nanostructures prepared at different dipping durations (c) 5 mins, (d) 10 mins, (e) 20 mins, and (f) 30 mins. (g) EDS mapping SEM image (h) s EDX spectra of the ZnO/CdS-30 nanostructures. Inset corresponds to the elemental composition estimated from EDX spectra (i-l) EDX elemental mapping showing the distribution of Zn (red), Oxygen (orange), Cd (blue), and S (green) for ZnO/CdS-30 nanostructures.

Transmission Electron Microscopy analysis

The synthesized ZnO NRs and then ZnO/CdS nanostructures were subsequently validated through low-resolution TEM and HRTEM analyses. Figures 4a and 4b present TEM images of ZnO NRs fabricated via electrochemical deposition. As discernible from Figures 4a and 5b, the ZnO exhibits a rod-like structure with a length spanning 1-2 µm and a diameter approximately 150-200 nm. Figure 4c reveals the selected area electron diffraction (SAED) pattern of ZnO NRs which showed the highly crystalline ZnO NRs with major (002) plane orientations and that can also be indexed to match that of the ZnO wurtzite lattice. The HRTEM image, as illustrated in Figure 4d, revealed clearly defined lattice fringes. These fringes, with a spacing of 0.52 nm, correspond to the

interplanar distance of the (002) plane of the hexagonal wurtzite structure of ZnO, with cell constants of a=3.2 Å and c=5.2 Å. This observation signifies the formation of the hexagonal phase of ZnO.

To understand the microscopic structure of the ZnO/CdS nanostructures, we also conducted a detailed investigation using low-resolution TEM and HRTEM. Figures 4e and 4f show TEM images of the interface between the ZnO/CdS nanostructures prepared for 30 mins dipping time. The TEM image unequivocally illustrates the synthesis of a ZnO/CdS nanostructures and the adherence of CdS NSs onto the surface of ZnO NRs. The alignment of CdS along the (111) plane can further be discerned from the Selected Area Electron Diffraction (SAED) pattern depicted in Figure 4g. This setup minimizes the charge diffusion length, allowing for effective electron collection and further decreasing the recombination loss of electron-hole pairs. Figure 4h presents a typical HRTEM image of a well-crystallized ZnO/CdS interface. The lattice fringe distance in the HRTEM is about 0.2 nm, which is consistent with the interplanar spacing of the (111) planes of CdS. Thus here, the NSs and NRs are linked with each other smoothly forming a good contact layer that should benefit the transfer of electrons from CdS to ZnO very easily.

PEC activity analysis

Linear sweep voltammetry

The linear sweep voltammetry (LSV) method was employed to assess the PEC cell performance of ZnO NRs, CdS NSs, and hybrid ZnO/CdS nanostructured photoelectrodes. The experimental procedures involved the use of a three-electrode cell, with a potential range of -0.6 V to 0.8 V versus a saturated calomel electrode (SCE). The electrolyte used in these measurements was a 0.5 M solution of sodium sulfate (Na_2SO_4). The photocurrent (I) as a function of the applied bias (V)

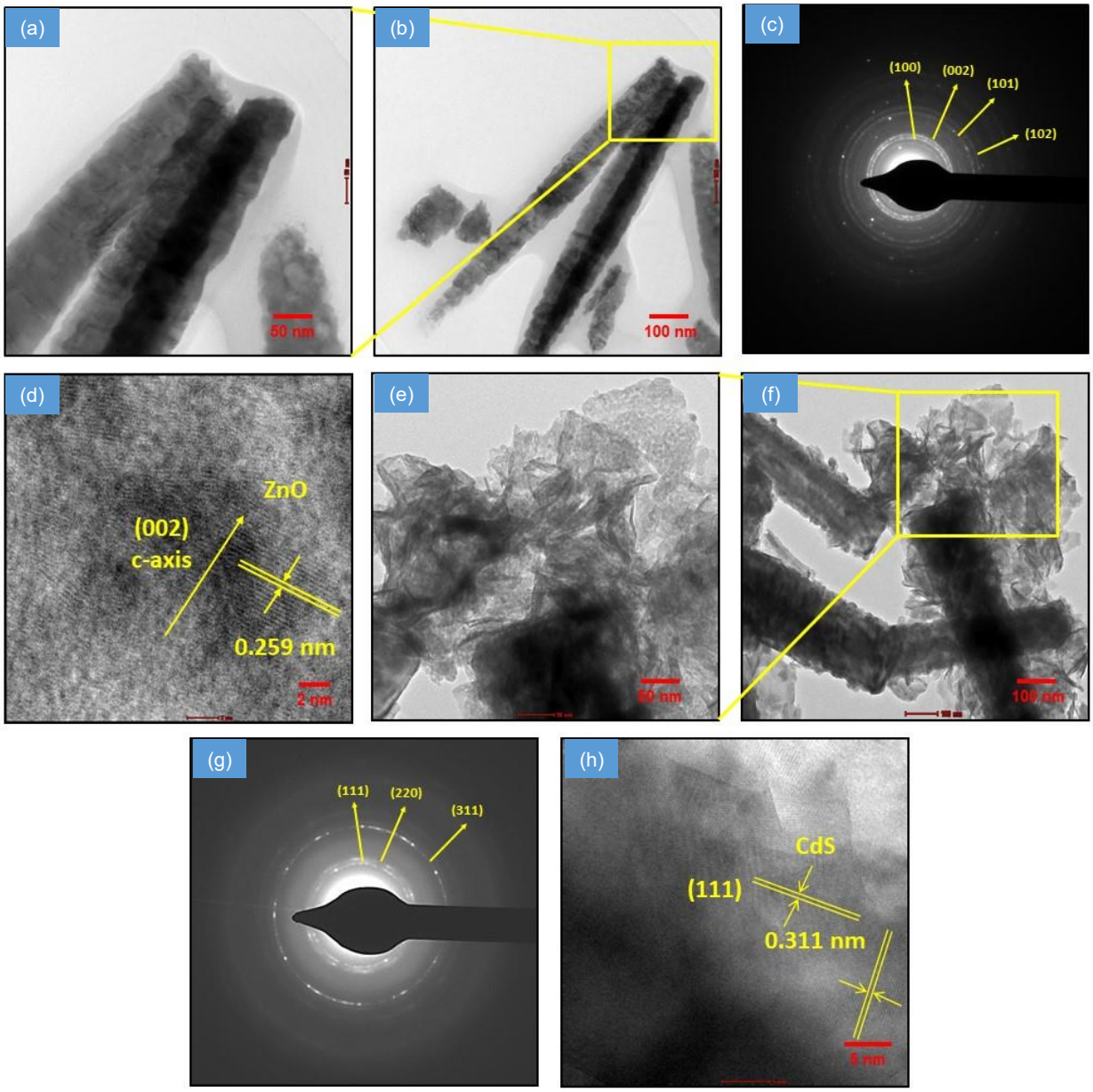

Figure 4. (a, b) Low resolution TEM pictures, (c) SAED pattern, (d) HRTEM image of ZnO NRs. (e, f) Low resolution TEM images, (g) SAED pattern, (h) HRTEM picture of the ZnO/CdS nanostructures interface.

is depicted in Figure 5a. During the dark-current measurements, a minimal current of approximately 0.01 μA/cm^2 was detected, attributable to non-faradic reactions. When subjected to light, ZnO experiences direct photoexcitation, leading to the creation of electron-hole pairs. The photo-induced electrons are propelled towards the platinum (Pt) counter electrode (cathode),

where they aid in the generation of hydrogen (H2) through proton reduction. Concurrently, the photo-generated holes react with water to yield oxygen (O_2). As evidenced by the PEC measurement presented in Figure 5a, the photocurrent density of ZnO NRs surpasses that of CdS NSs. This is due to the higher bulk carrier diffusion length of ZnO[65] as compared to CdS.[66] Therefore, the recombination of photogenerated carriers is prevented and the transport of carriers is enhanced. However, due to the wide bandgap of ZnO-NRs, the visible light absorption of the solar spectrum becomes difficult whereas CdS-NSs offer much faster carrier transport compared to its bulk counterpart. Both objectives of fast carrier transport as well as harvesting solar spectrum efficiently can be achieved by fabricating ZnO-NRs/CdS-NSs nanostructures. The schematic of the charge transport across the CdS/ZnO nanostructures is shown in Figure 5d. The carrier transport mechanisms during the PEC water splitting using CdS/ZnO nanostructures as photoelectrode under light irradiation is shown in Figure 5e. In the presence of light, CdS produces photo generated electrons-hole pairs. All the photogenerated electrons may not participate in the PEC reduction due to its fast recombination with holes. However, in the CdS/ZnO nanostructure, the photo-induced electrons are swiftly conveyed to the ZnO NRs. This rapid transfer mitigates the recombination of electron-hole pairs, thereby bolstering the efficiency of the PEC water splitting process.

The ZnO/CdS nanostructures fabricated with increasing dipping time showed a gradual increase in photocurrent density and the highest ABPE of ~ 0.63 % has been obtained for ZnO/CdS-30 sample with photocurrent density of ~ 1.87 mA/cm^2. The % of ABPE has been calculated for the photo-electrodes using the Equation below.

$$\mathrm{ABPE} = \frac{J_{Ph}\ (1.23 - |V_{Bias}|)}{P_{Light}} \qquad (4)$$

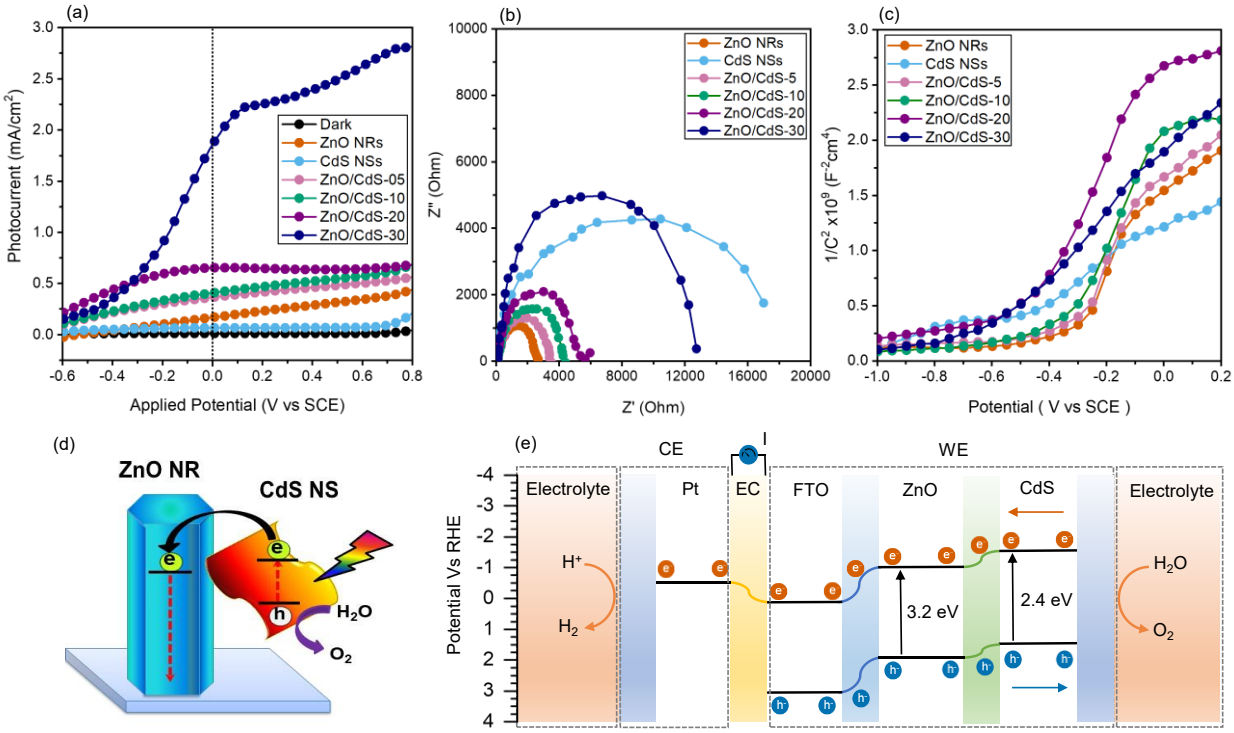

Figure 5. (a) Difference in photocurrent density as a function of the applied potential for ZnO-NRs, CdS-NSs, and ZnO/CdS hetero-structures prepared at different dipping durations (b) Nyquist plots obtained from the electrochemical impedance spectra of ZnO-NRs, CdS-NSs, and ZnO/CdS hetero-structures prepared at different dipping durations. The inset provides a depiction of the equivalent circuit model pertinent to the electrochemical impedance spectra. (c) Mott-Schottky curves of for ZnO-NRs, CdS-NSs, and ZnO/CdS nanostructures prepared at different dipping durations. (d) Schematic of CdS/ZnO nanostructures (e) Carrier Transport Mechanisms during the photoelectrochemical water splitting using CdS/ZnO nanostructures as photoelectrode under light irradiation.

where J_{Ph} represents the photocurrent density, measured in mA/cm^2, V_{Bias} is the externally applied potential, and P_{Light} denotes the intensity of the light source's illumination.[67] The calculated efficiency parameters for ZnO NRs, CdS NSs, and the ZnO/CdS photo-electrode are listed in Table 1.

Despite the better carrier lifetime of CdS, the photocurrent density and apparent photon-to-current conversion efficiency (ABPE) of ZnO/CdS-5 are better than that of CdS due to several reasons. One reason could be the formation of a heterojunction in the ZnO/CdS-5 system, which can enhance the separation of photogenerated charge carriers, thereby reducing recombination and

increasing photocurrent.[32] Moreover, the ZnO/CdS-5 system might have a more favorable band alignment or surface properties that enhance photocatalytic activity.[68–71] As observed, the incorporation of CdS NSs with ZnO NRs enhances light absorption, thereby enhancing the photocurrent conversion efficiency. Consequently, the ZnO/CdS nanostructures emerge as a potential candidate for efficient PEC water splitting. Notably, the fabricated ZnO NRs, CdS NSs, and ZnO/CdS nanostructure photoelectrodes exhibited stability, even after numerous scans, with no observable physicochemical degradation, affirming the robustness of these systems for water splitting reactions. The stability test of the ZnO/CdS photoanodes provides valuable information about the long-term performance of the photoanode. Although the photo-response stability test for our prepared photoanodes is not performed, there are few reports demonstrating ZnO/CdS heterostructure stability up to 20 hours.[22,72]

Electrochemical impedance spectroscopy analysis

To elucidate the PEC behavior of the engineered photoanodes, we conducted an analysis using EIS within a frequency spectrum of 0.1 Hz to 100 kHz, at a bias of 0 V versus SCE, under UV-Visible light exposure. The Nyquist plot, extracted from the EIS data, acts as an effective instrument for evaluating the resistance to electron transfer. The arc's radius in the Nyquist plot is inherently connected to the resistance to electron transfer, thus reflecting the energy barrier tied to the electrode reaction.[73] Figure 5b presents the EIS measurements, depicted via Nyquist plots, with the inset illustrating the corresponding equivalent circuit model for the EIS spectra. To discern the impact of CdS NSs, the Nyquist plot incorporates the ZnO/CdS nanostructured photoanodes, both with and without the CdS NSs' layer. As per the equivalent circuit model, the ohmic resistance, denoted as Rs, is associated with the resistance between the FTO and the electrolyte. The EIS

Table 1. Efficiency parameters for ZnO-NRs, CdS-NSs and ZnO/CdS hetero-structures photoelectrode

Samples	Photocurrent density, J_{ph} (mA/cm^2)	ABPE or PEC (%)
ZnO-NRs	0.17	0.06
CdS-NSs	0.07	0.03
ZnO/CdS-5	0.37	0.12
ZnO/CdS-10	0.41	0.14
ZnO/CdS-20	0.65	0.22
ZnO/CdS-30	1.87	0.63

analysis revealed that this resistance was at its minimum for all the samples under consideration. The semicircular feature observed in the Nyquist plot corresponds to the charge transfer resistance (Rct) at the interface between ZnO/CdS and the electrolyte. The Constant Phase Element symbolizes the capacitance element that is in phase with Rct. A smaller Rct corresponds to a low recombination rate, and the prolonged lifetime of photogenerated charge carriers.[74] ZnO exhibits excellent electron accepting properties, coupled with a high electron mobility of approximately 155 cm^2/Vs.[65] Consequently, it can efficiently curtail the resistance to charge transfer and diminish the recombination of photo-induced charge carriers.[74] As discerned from Figure 5b, the arc radii for the ZnO/CdS photoanodes are notably smaller compared to those of the individual CdS NSs. This observation indicates that the deposition of CdS-NSs onto the surface of ZnO NRs significantly augments the efficiency of separation and transfer of the photo-induced electron-hole pairs, attributable to the interfacial interaction between the CdS-NSs and ZnO-NRs phases. The ZnO-NRs accept and convey the photo-generated electrons from the CdS-NSs, while also offering

active sites on their surface for the evolution of hydrogen. The photo-generated electron traverses a continuous path to the counter electrode, devoid of recombination. The lifecycle of the electron culminates upon reaching the electrolyte.[75] Consequently, the impedance circle of the engineered photoanodes exhibits a substantial reduction, signifying a marked decrease in the resistance to charge transfer. Here, the charge transfer resistance of the FTO/ZnO (2463 Ω) electrode is much smaller than the FTO/CdS electrode (17263 Ω). Similar results have been reported by Han et al.[76] for vertically aligned $AgSbS_2$ modified ZnO nanotube arrays for PEC water splitting and by Wu et al.[77] for a multi-layered TiO_2 photoanode with hyper-branched TiO_2 architecture for DSSCs or QDSSCs.

The electron lifetime (τ) is also calculated from the Bode imaginary plot by using the below equation,

$$\tau = \frac{1}{2\pi f_{peak}} \quad (5)$$

where, f_{peak} is the characteristic peak frequency mid-frequency range (1-100) Hz at which the imaginary part is at its maximum. The prolonged lifetime of photogenerated carriers of ZnO NRs photoanodes implies faster separation, transport, and collection compared with CdS-NSs. The ZnO/CdS nanostructure photoanodes showed a significant increase in the carrier lifetime confirming the longer separation and transport of electrons and holes as seen from Table 2. Thus, the effective recombination reduction of the photo-generated charge carriers causes an improvement in photocatalytic efficiency. After the deposition of CdS NSs layer on the FTO/ZnO electrode for different dipping time (from 5 mins to 30 mins) the diameter of the semicircle in the Nyquist plot increased showing an increase in charge transfer resistance (Rct) but it remained much smaller than that of the FTO/CdS electrode. The increase in charge transfer resistance with

CdS deposition time is due to an increase in CdS blockage layer for transfer of an electron between the interface of FTO/ZnO photoelectrode and electrolyte. Thus, the effective reduction in the charge transfer resistance in the FTO/CdS electrode is achieved after the introduction of ZnO NRs between them as observed from the electrochemical impedance spectra in Figure 5b. Ideally, a lower charge transfer resistance should correspond to a higher photocurrent. The photocurrent trend and the charge transfer resistance obtained from EIS data can sometimes show different trends due to the different processes they represent in a PEC system.[78–80] The photocurrent is a measure of the photogenerated charge that is collected at the electrodes in a PEC system.[81] It is governed by parameters such as the proficiency of light absorption by the photoanode, the effectiveness of charge separation at the interface between the photoanode and the electrolyte, and the efficiency of charge accumulation at the electrodes.[81] Conversely, the charge transfer resistance (Rct), as determined from EIS, serves as a tool for approximating the kinetics of the redox reactions occurring on the surface of the electrode material.[80] It signifies the resistance encountered by the charge as it traverses the interface between the electrode and the electrolyte.[79] A diminished Rct signifies enhanced kinetics of the redox reactions occurring on the surface of the electrode material.[80] Hence, while the photocurrent serves as an indicator of the comprehensive efficiency of the PEC process, the charge transfer resistance offers specific insights into the kinetics of the redox reactions occurring at the interface between the electrode and the electrolyte. Differences in these two measures can arise due to differences in the efficiencies of the various processes involved in the PEC system.[78–81]

Mott-Schottky analysis

Figure 5c shows the Mott-Schottky (MS) curves for as-synthesized ZnO-NRs, CdS-NSs, and created ZnO/CdS nanostructure photoanodes. As can be seen from Figure 5c all curves exhibited

Table 2: Numerical Values of the electrochemical impedance spectra for different synthesized samples.

Samples	Series Resistance R_s (Ω)	Charge Transfer Resistance Rct(Ω)	CPE (μF)	Carrier Lifetime τ (ms)	Phase Θ (º)
ZnO-NRs	87	2463	17.88	30.75	69.5
CdS-NSs	168	17263	23.04	19.98	81.7
ZnO/CdS-5	87	3393	13.80	7.51	68.8
ZnO/CdS-10	119	4199	15.75	40.76	70.5
ZnO/CdS-20	80	5034	16.21	54.03	74.0
ZnO/CdS-30	115	12095	20.82	166.91	80.4

positive slopes, indicating their n-type nature. The parameters such as the flat band potential (V_{fb}), slope, charge carrier density (N_d), and depletion width (w) can be deduced from the Mott-Schottky curves. These calculations utilize the capacitance (C) measured at the semiconductor/electrolyte interface with respect to different potential (V) values by using the following equations:[82,34]

$$\frac{1}{C^2} = \frac{2}{q\,\varepsilon_0\,\varepsilon_s N_D}\left[(V - V_{fb})\frac{k_B T}{q}\right] \quad (6)$$

$$S = \frac{2}{q\,\varepsilon_0\,\varepsilon_s N_D} \quad (7)$$

$$w = \left[\frac{2\,\varepsilon_s\,\varepsilon_0}{q\,N_D}(V - V_{fb})\right]^{1/2} \quad (8)$$

In these equations, q denotes the electronic charge, ε_0 is the permittivity of free space, ε_s is the dielectric constant of the semiconductor electrode (approximately 5.7 at low frequencies less than MHz),[83,84] k_B is Boltzmann's constant, T is the temperature (expressed in Kelvin), S is the slope of

Table 3: The flat band potential (V_{fb}), slope, donor density (N_d), and width of the depletion layer (w) for various fabricated samples.

Samples	Flat band potential V_{fb} (V vs SCE)	Slope ($F^{-2}cm^4V$)	Charge Carrier Density N_d (cm^{-3})	Depletion layer width (nm)
ZnO NRs	-0.31	$6.91x10^{10}$	$2.36x\ 10^{17}$	24.79
CdS NSs	-0.64	$2.15x10^{10}$	$7.59x\ 10^{18}$	15.44
ZnO/CdS-5	-0.33	$6.84x10^{10}$	$2.38x\ 10^{18}$	24.88
ZnO/CdS-10	-0.46	$6.00x10^{10}$	$2.72x\ 10^{18}$	24.41
ZnO/CdS-20	-0.51	$5.72x10^{10}$	$2.85x\ 10^{18}$	24.21
ZnO/CdS-30	-0.61	$3.21x10^{10}$	$5.08\ x\ 10^{18}$	18.75

the Mott-Schottky curve, and w is the width of the depletion layer. The values of the flat band potential (V_{fb}) are determined by extrapolating the linear portion of the $1/C^2$ plot to the x-axis.

Table 3 presents the values of the flat band potential (V_{fb}), slope, donor density (N_d), and depletion layer width (w) for various synthesized samples, including ZnO NRs, CdS NSs, and ZnO/CdS. The N_d values, derived from the Mott-Schottky plots, are contingent on the surface area of the samples exposed to the electrolyte. Consequently, the N_d values in this study offer a comparative analysis between ZnO NRs and CdS NSs loaded ZnO NRs. As inferred from the table, more negative V_{fb} values indicate a decrease in the recombination rate, coupled with an enhancement in charge separation and transport at the semiconductor/electrolyte junction. Additionally, a significant change is observed in the flat bandpotential values, from -0.31 V/SCE for the ZnO-NRs to -0.61 V/SCE for the ZnO/CdS-30 nanostructure photoanode. It is noted that N_d escalated

from 2.36×10^{17} cm^{-3} for ZnO-NRs to 5.08×10^{18} cm^{-3} for the ZnO/CdS-30 nanostructure photoanode, attributable to enhanced conductivity, a trait conducive to PEC activity.

DFT Results

Lattice parameters and stability

The unit cell of ZnO contains two and that of CdS one formula unit per simulation cell. The computed lattice parameters are given in Table 4.[85–90] The PBE0 functional is found to reproduce the experimental lattice parameters very well, within deviations smaller than 1%. The phonon dispersions calculated within the first Brillouin zone for ZnO and CdS are shown in Figures 5a and 5b. All frequencies have positive values, satisfying the crystal stability condition where the lattice needs to be stable with respect to small atomic displacements.[91] This further supports the stability of the individual synthesized compounds at ambient pressure. From the phonon densities of state, it is noted that in both analyzed compounds the transition metal contributes almost entirely to the vibrational spectrum at low frequencies, while the ligands vibrate with higher frequencies separated by a phonon gap.

Electronic structure and band alignment

The calculated single-particle Kohn-Sham electronic band structure of CdS and ZnO is shown in Figures 6c and 6d. Both materials exhibit a direct electronic band gap situated at the Γ-point in the reciprocal space. The apex of valence band (VB) is predominantly made of d-states derived from the transition metal, with a minor overlap with the p-states of sulphur in CdS and oxygen in ZnO, respectively.

Table 4: DFT computed lattice parameters and electronic band gap of ZnO and CdS in comparison with available experimental data. Values are reported using two different methodologies, employing plane-waves (PAW) and using all-electron (AE) calculations.

Method	ZnO (wurtzite)			CdS (cubic)	
	a (Å)	c (Å)	Eg (eV)	a (Å)	Eg (eV)
PBE0 (PAW)	3.2510	5.2231	3.49	5.8859	2.59
PBE0 (AE)	3.2672	5.2001	3.16	5.8943	2.74
Experiment	3.25 [85]	5.21 [85]	3.25 - 3.4 [86,87]	5.82 [88]	2.3 - 2.5 [89,90]

The obtained electronic band gap values (listed in Table 4) correspond well to the experimentally obtained UV-Visible spectroscopic data. The charge carrier effective masses computed along different directions along 1-dimentional ribbons starting at the Γ-point are given in Table 5. The conductivity of ZnO is mostly isotropic, as neither the electron nor the hole effective masses differ greatly along different crystallographic directions. While the electron effective masses are similar in the Γ-to-K and Γ-to-L directions of CdS, a 2.5 times larger electron effective mass is noted in the Γ-to-X direction (which corresponds to the direction along the crystallographic y-axis). Hole effective masses of CdS are largely isotropic. Since the effective mass is inversely proportional to the carrier mobility and hence conductivity,[92] holes are expected to be mobile in both ZnO as well as CdS. The electron conductivity is somewhat enhanced in CdS when compared to ZnO, but only in the aforementioned Γ-to-K and Γ-to-L directions of the crystal. The Γ-to-X path does not indicate a favorable route for electron transfer.

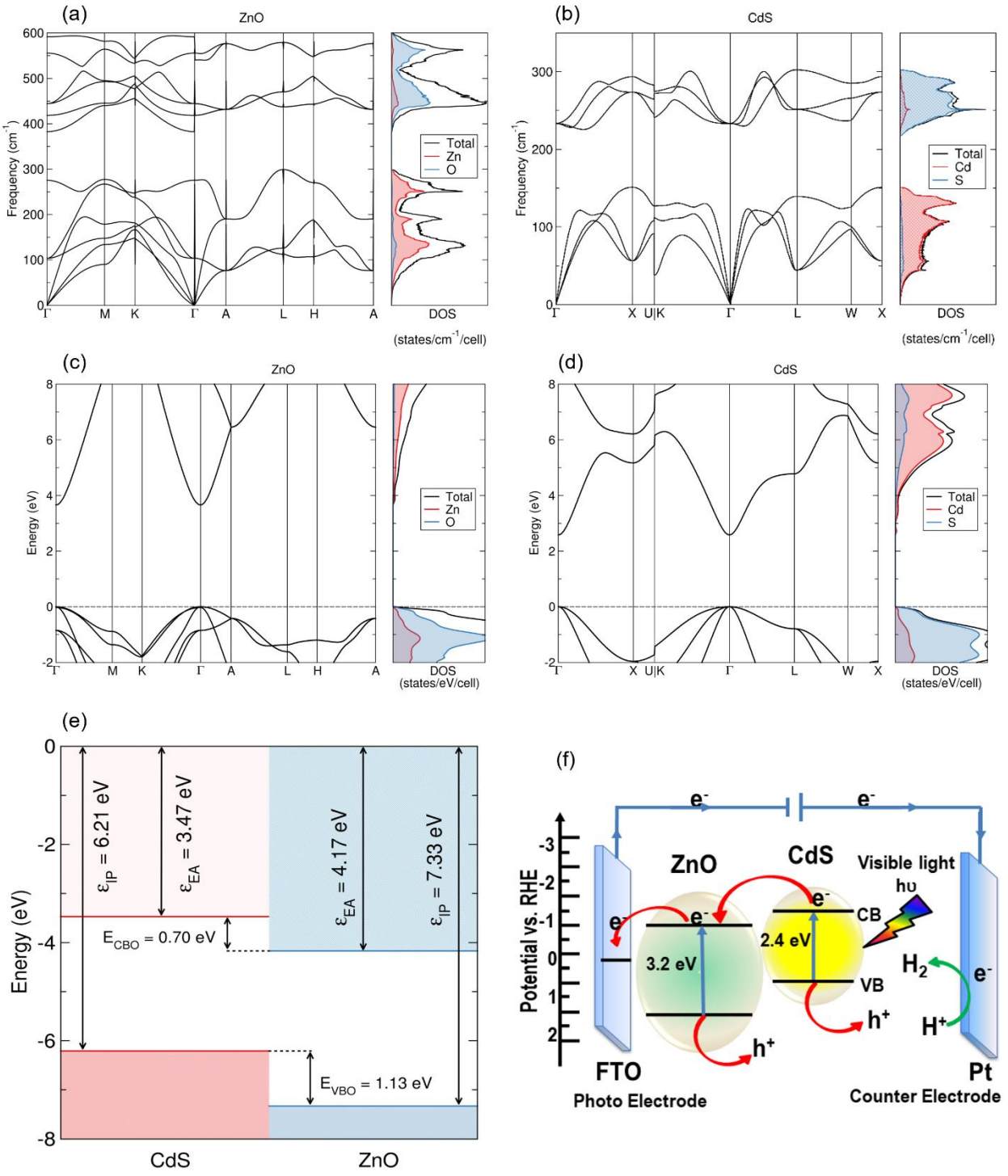

Figure 6. (a and b) Phonon dispersion curves together with corresponding (total and atom projected) phonon densities of state of ZnO and CdS, calculated using PBE0 (AE basis) (c and d) Electronic band structure represented in conjunction with the aggregate and atomically projected electronic densities of states for ZnO and CdS, computed utilizing the PBE0 method (AE basis). The dashes line indicates the highest occupied state (e) Schematic representation of calculated band alignment of CdS and ZnO, based

on the ionization potential and electron affinity obtained using PBE0 (PAW) (f) PEC water splitting mechanism of CdS/ZnO nanostructure under light irradiation.

At the PBE0 (PAW) level of theory, the calculated surface energies of ZnO(100), CdS(110), and CdS(111) read 0.89 J/m^2, 0.41 J/m^2, and 0.53 J/m^2, respectively, thus indicating their likely presence in the nanoparticles from a favourable energetic perspective. The (bulk based) IP is calculated at 10.53 eV for ZnO and 9.59 eV for CdS (9.31 eV in the reconstructed slab), respectively. Together with the calculated EA (7.37 eV for ZnO and 6.85 eV CdS (6.58 eV in the reconstructed case)), a type-II band staggered band alignment is observed for a heterojunction based on these two materials. In addition, the favourable VB and CB offsets indicate a viable and efficient transport route for the photo-generated electrons to transfer from CdS to ZnO and conversely for generate holes to flow from ZnO to CdS, as shown in Figure 6c. It should be noted that this model considers only the positions of the fundamental band edges and ignores any effects arising from strain of chemical interactions at the interface. However, even at a such crude level, it corroborates the experimental findings outlined earlier and opens-up a route of possible interpretation of the results obtained for the ZnO/CdS nanostructure [93].

Table 5: The effective masses of electrons and holes determined at the PBE0 (PAW) theoretical level. The reported values are expressed in terms of the mass of a free electron (m_0).

	Effective mass (m_0)			
	Valence band		Conduction band	
ZnO	$\Gamma \rightarrow M$	-2.522	$\Gamma \rightarrow M$	0.238
	$\Gamma \rightarrow K$	-2.631	$\Gamma \rightarrow K$	0.230
	$\Gamma \rightarrow A$	-2.631	$\Gamma \rightarrow A$	0.230
	$\Gamma \rightarrow X$	-4.144	$\Gamma \rightarrow X$	0.163
CdS	$\Gamma \rightarrow K$	-1.628	$\Gamma \rightarrow K$	0.162
	$\Gamma \rightarrow L$	-1.537	$\Gamma \rightarrow L$	0.163

CONCLUSIONS

The successful synthesis of ZnO/CdS nanostructures was achieved through a simple two-step chemical process, specifically electrodeposition and chemical bath deposition. The preparation of ZnO NRs, CdS NSs, and ZnO/CdS nanostructures has been validated by XRD, Raman spectroscopy, SEM, HRTEM, and UV-Visible absorption spectroscopy. The performance of the fabricated nanostructures in PEC water splitting was examined using linear sweep voltammetry, Mott-Schottky analysis, and electrochemical impedance spectroscopy. The results suggest that the efficiency of photocurrent conversion in the water splitting process is higher for the ZnO/CdS photoanode as compared to the isolated ZnO NRs photoanodes. The data implies that the integration of CdS NSs with ZnO NRs contributes positively to the augmentation of light absorption and the enhancement of photocurrent conversion efficiency during water splitting. Consequently, the configuration of the ZnO/CdS nanostructure emerges as a potential contender

for efficient PEC water splitting. The highest photoconversion efficiency of 2.3 % is obtained for ZnO/CdS nanostructures that can be used in the production of hydrogen fuel via water splitting.

AUTHOR INFORMATION

Corresponding Authors

**Avinash Rokade*

Department of Physics, Savitribai Phule Pune University, Pune 411007, India.

Email: avrokade88@gmail.com

**Sandesh R. Jadkar*

Department of Physics, Savitribai Phule Pune University, Pune 411007, India.

Email: sandesh@physics.unipune.ac.in

**Sachin R. Rondiya*

Department of Materials Engineering, Indian Institute of Science, Bangalore 560012, India

Email: rondiya@iisc.ac.in

Authors

Avinash Rokade

Department of Physics, Savitribai Phule Pune University, Pune 411007, India

Ganesh K. Rahane

Department of Materials Engineering, Indian Institute of Science, Bangalore 560012, India

Aleksandar Živković

Department of Earth Sciences, Utrecht University, Princetonlaan 8a, 3548CB Utrecht, The Netherlands

Swati N. Rahane

Department of Physics, Savitribai Phule Pune University, Pune 411007, India

Hemant S. Tarkas

Department of Physics, Savitribai Phule Pune University, Pune 411007, India

K. Hareesh

Department of Physics, Manipal Institute of Technology Bengaluru, Manipal Academy of Higher Education, Manipal 576104, India

Nora H. de Leeuw

Department of Earth Sciences, Utrecht University, Princetonlaan 8a, 3548CB Utrecht, The Netherlands

School of Chemistry, University of Leeds, Leeds LS2 9JT, United Kingdom

Shrikrishna Dattatraya Sartale

Department of Physics, Savitribai Phule Pune University, Pune 411007, India

Nelson Y. Dzade

Department of Energy and Mineral Engineering, Pennsylvania State University, University Park, Pennsylvania 16802, United States

Funding Sources

AR and HST thank SPPU PDF (Grant No. SPPUPDF/ST/PH/2021/0005 and PDF/ST/PH/2021/0009) for financial support. SRJ is thankful to the University Grants Commission (UPE program), New Delhi, and Indo-French Centre for the Promotion of Advanced Research-CEFIPRA, Department of Science and Technology, New Delhi for special financial support. GKR and SRR acknowledges the support of the Department of Materials Engineering, Indian Institute of Science (IISc), Bangalore, India. SNR is thankful to the Chhatrapati Shahu Maharaj Research Training and Human Development Institute (SARTHI) for the financial support (CSMNRF-2021). NYD acknowledges the support of the College of Earth and Minerals Sciences and the John and Willie Leone Family Department of Energy and Mineral Engineering of the Pennsylvania State University. NYD also acknowledges the UK Engineering and Physical Sciences Research Council (EPSRC) funding (Grant No. EP/S001395/1). AŽ and NL acknowledge the NWO ECHO grant (712.018.005) for funding.

ACKNOWLEDGMENT

AR and HST thank SPPU PDF (Grant No. SPPUPDF/ST/PH/2021/0005 and PDF/ST/PH/2021/0009) and Department of Physics, SPPU, for financial support and laboratory facilities access. SRJ is thankful to the University Grants Commission (UPE program), New Delhi, and Indo-French Centre for the Promotion of Advanced Research-CEFIPRA, Department of Science and Technology, New Delhi for special financial support. GKR and SRR acknowledges the support of the Department of Materials Engineering, Indian Institute of Science (IISc), Bangalore, India. SNR is thankful to the Chhatrapati Shahu Maharaj Research Training and Human Development Institute (SARTHI) for the financial support (CSMNRF-2021). We are thankful to Balpratap Singh for the help in preparation of the table of content figure. NYD acknowledges the support of the College of Earth and Minerals Sciences and the John and Willie Leone Family Department of Energy and Mineral Engineering of the Pennsylvania State University. NYD also acknowledges the UK Engineering and Physical Sciences Research Council (EPSRC) funding (Grant No. EP/S001395/1). Via our membership of the UK's HEC Materials Chemistry Consortium, which is funded by EPSRC (EP/R029431), this work used the ARCHER2 United Kingdom National Supercomputing Service (http://www.archer2.ac.uk). AŽ and NL acknowledge the NWO ECHO grant (712.018.005) for funding. We thank SURF (www.surf.nl) for the support in using the National Supercomputer Snellius.

CONFLICT OF INTERESTS

The authors declare no conflict of interest.

REFERENCES

(1) Hussain, A.; Arif, S. M.; Aslam, M. Emerging Renewable and Sustainable Energy Technologies: State of the Art. *Renewable and Sustainable Energy Reviews* **2017**, *71* (June 2015), 12–28. https://doi.org/10.1016/j.rser.2016.12.033.

(2) Owusu, P. A.; Asumadu-Sarkodie, S. A Review of Renewable Energy Sources, Sustainability Issues and Climate Change Mitigation. *Cogent Eng* **2016**, *3* (1), 1–14. https://doi.org/10.1080/23311916.2016.1167990.

(3) Ager, J. W.; Shaner, M. R.; Walczak, K. A.; Sharp, I. D.; Ardo, S. Experimental Demonstrations of Spontaneous, Solar-Driven Photoelectrochemical Water Splitting. *Energy Environ Sci* **2015**, *8* (10), 2811–2824. https://doi.org/10.1039/c5ee00457h.

(4) Ros, C.; Andreu, T.; Morante, J. R. Photoelectrochemical Water Splitting: A Road from Stable Metal Oxides to Protected Thin Film Solar Cells. *J Mater Chem A Mater* **2020**, *8* (21), 10625–10669. https://doi.org/10.1039/d0ta02755c.

(5) Li, Z.; Luo, W.; Zhang, M.; Feng, J.; Zou, Z. Photoelectrochemical Cells for Solar Hydrogen Production: Current State of Promising Photoelectrodes, Methods to Improve Their Properties, and Outlook. *Energy Environ Sci* **2013**, *6* (2), 347–370. https://doi.org/10.1039/c2ee22618a.

(6) Walter, M. G.; Warren, E. L.; McKone, J. R.; Boettcher, S. W.; Mi, Q.; Santori, E. A.; Lewis, N. S. Solar Water Splitting Cells. *Chem Rev* **2010**, *110* (11), 6446–6473. https://doi.org/10.1021/cr1002326.

(7) Nakata, K.; Fujishima, A. TiO 2 Photocatalysis: Design and Applications. *Journal of Photochemistry and Photobiology C: Photochemistry Reviews* **2012**, *13* (3), 169–189. https://doi.org/10.1016/j.jphotochemrev.2012.06.001.

(8) Bera, A.; Wu, K.; Sheikh, A.; Alarousu, E.; Mohammed, O. F.; Wu, T. Perovskite Oxide SrTiO3 as an Efficient Electron Transporter for Hybrid Perovskite Solar Cells. *Journal of Physical Chemistry C* **2014**, *118* (49), 28494–28501. https://doi.org/10.1021/jp509753p.

(9) Yang, W.; Yu, Y.; Starr, M. B.; Yin, X.; Li, Z.; Kvit, A.; Wang, S.; Zhao, P.; Wang, X. Ferroelectric Polarization-Enhanced Photoelectrochemical Water Splitting in TiO2-BaTiO3 Core-Shell Nanowire Photoanodes. *Nano Lett* **2015**, *15* (11), 7574–7580. https://doi.org/10.1021/acs.nanolett.5b03988.

(10) Wolcott, A.; Smith, W. A.; Kuykendall, T. R.; Zhao, Y.; Zhang, J. Z. Photoelectrochemical Study of Nanostructured Zno Thin Films for Hydrogen Generation from Water Splitting. *Adv Funct Mater* **2009**, *19* (12), 1849–1856. https://doi.org/10.1002/adfm.200801363.

(11) Hsiao, P. T.; Chen, L. C.; Li, T. L.; Teng, H. Vapor Treatment of Nanocrystalline WO3 Photoanodes for Enhanced Photoelectrochemical Performance in the Decomposition of Water. *J Mater Chem* **2011**, *21* (48), 19402–19409. https://doi.org/10.1039/c1jm14785d.

(12) Khan, S. U. M.; Akikusa, J. Photoelectrochemical Splitting of Water at Nanocrystalline N-Fe2O3 Thin-Film Electrodes. *Journal of Physical Chemistry B* **1999**, *103* (34), 7184–7189. https://doi.org/10.1021/jp990066k.

(13) Sun, K.; McDowell, M. T.; Nielander, A. C.; Hu, S.; Shaner, M. R.; Yang, F.; Brunschwig, B. S.; Lewis, N. S. Stable Solar-Driven Water Oxidation to O2(G) by Ni-Oxide-Coated Silicon Photoanodes. *Journal of Physical Chemistry Letters* **2015**, *6* (4), 592–598. https://doi.org/10.1021/jz5026195.

(14) Wang, M.; Ren, F.; Zhou, J.; Cai, G.; Cai, L.; Hu, Y.; Wang, D.; Liu, Y.; Guo, L.; Shen, S. N Doping to ZnO Nanorods for Photoelectrochemical Water Splitting under Visible Light: Engineered Impurity Distribution and Terraced Band Structure. *Sci Rep* **2015**, *5* (August), 1–13. https://doi.org/10.1038/srep12925.

(15) Hsu, Y. K.; Lin, Y. G.; Chen, Y. C. Polarity-Dependent Photoelectrochemical Activity in ZnO Nanostructures for Solar Water Splitting. *Electrochem commun* **2011**, *13* (12), 1383–1386. https://doi.org/10.1016/j.elecom.2011.08.016.

(16) Chandiran, A. K.; Abdi-Jalebi, M.; Nazeeruddin, M. K.; Grätzel, M. Analysis of Electron Transfer Properties of ZnO and TiO2 Photoanodes for Dye-Sensitized Solar Cells. *ACS Nano* **2014**, *8* (3), 2261–2268. https://doi.org/10.1021/nn405535j.

(17) Zhang, X.; Chen, Y. L.; Liu, R. S.; Tsai, D. P. Plasmonic Photocatalysis. *Reports on Progress in Physics* **2013**, *76* (4). https://doi.org/10.1088/0034-4885/76/4/046401.

(18) Wang, C.; Chen, Z.; Jin, H.; Cao, C.; Li, J.; Mi, Z. Enhancing Visible-Light Photoelectrochemical Water Splitting through Transition-Metal Doped TiO2 Nanorod Arrays. *J Mater Chem A Mater* **2014**, *2* (42), 17820–17827. https://doi.org/10.1039/c4ta04254a.

(19) Warren, S. C.; Thimsen, E. Plasmonic Solar Water Splitting. *Energy Environ Sci* **2012**, *5* (1), 5133–5146. https://doi.org/10.1039/c1ee02875h.

(20) Solanki, A.; Shrivastava, J.; Upadhyay, S.; Sharma, V.; Sharma, P.; Kumar, P.; Kumar, P.; Gaskell, K.; Satsangi, V. R.; Shrivastav, R.; Dass, S. Irradiation-Induced Modifications and PEC Response - A Case Study of SrTiO3 Thin Films Irradiated by 120 MeV Ag9+ Ions. *Int J Hydrogen Energy* **2011**, *36* (9), 5236–5245. https://doi.org/10.1016/j.ijhydene.2011.01.149.

(21) Theys, B.; Sallet, V.; Jomard, F.; Lusson, A.; Rommeluère, J. F.; Teukam, Z. Effects of Intentionally Introduced Hydrogen on the Electrical Properties of ZnO Layers Grown by Metalorganic Chemical Vapor Deposition. *J Appl Phys* **2002**, *91* (6), 3922–3924. https://doi.org/10.1063/1.1452778.

(22) Chen, J.; Zhao, D. W.; Lei, W.; Sun, X. W. Cosensitized Solar Cells Based on a Flower-like ZnO Nanorod Structure. *IEEE Journal on Selected Topics in Quantum Electronics* **2010**, *16* (6), 1607–1610. https://doi.org/10.1109/JSTQE.2009.2037831.

(23) Fang, X.; Bando, Y.; Gautam, U. K.; Zhai, T.; Zeng, H.; Xu, X.; Liao, M.; Golberg, D. *ZnO and ZnS Nanostructures: Ultraviolet-Light Emitters, Lasers, and Sensors*; 2009; Vol. 34. https://doi.org/10.1080/10408430903245393.

(24) Yi, G.-C.; Yoo, J.; Park, W. Il; Jung, S. W.; An, S. J.; Kim, H. J.; Kim, D. W. ZnO Nanorods for Electronic and Photonic Device Applications. In *Nanostructure Integration Techniques for Manufacturable Devices, Circuits, and Systems: Interfaces, Interconnects, and Nanosystems*; Freund, M. M., Islam, M. S., Dutta, A. K., Eds.; 2005; Vol. 6003, p 600301. https://doi.org/10.1117/12.637952.

(25) Azzez, S. A.; Hassan, Z.; Hassan, J. J.; Mukhlif, M. S.; Mahdi, M. S.; Bououdina, M. Effect of Temperature on Hydrothermally Grown High-Quality Single-Crystals Mg-Doped ZnO Nanorods for Light-Emitting Diode Application. *J Lumin* **2017**, *192* (December 2016), 634–643. https://doi.org/10.1016/j.jlumin.2017.07.050.

(26) Yin, Z.; Wu, S.; Zhou, X.; Huang, X.; Zhang, Q.; Boey, F.; Zhang, H. Electrochemical Deposition of ZnO Nanorods on Transparent Reduced Graphene Oxide Electrodes for Hybrid Solar Cells. *Small* **2010**, *6* (2), 307–312. https://doi.org/10.1002/smll.200901968.

(27) Wang, Z. L. Zinc Oxide Nanostructures: Growth, Properties and Applications. *Journal of Physics Condensed Matter* **2004**, *16* (25). https://doi.org/10.1088/0953-8984/16/25/R01.

(28) Ahn, K. S.; Shet, S.; Deutsch, T.; Jiang, C. S.; Yan, Y.; Al-Jassim, M.; Turner, J. Enhancement of Photoelectrochemical Response by Aligned Nanorods in ZnO Thin Films. *J Power Sources* **2008**, *176* (1), 387–392. https://doi.org/10.1016/j.jpowsour.2007.10.034.

(29) Ahmed, F.; Arshi, N.; Anwar, M. S.; Danish, R.; Koo, B. H. Morphological Evolution of ZnO Nanostructures and Their Aspect Ratio-Induced Enhancement in Photocatalytic Properties. *RSC Adv* **2014**, *4* (55), 29249–29263. https://doi.org/10.1039/c4ra02470b.

(30) Yang, X.; Wolcott, A.; Wang, G.; Sobo, A.; Fitzmorris, R. C.; Qian, F.; Zhang, J. Z.; Li, Y. Nitrogen-Doped ZnO Nanowire Arrays for Photoelectrochemical Water Splitting. *Nano Lett* **2009**, *9* (6), 2331–2336. https://doi.org/10.1021/nl900772q.

(31) Yu, Q.; Cao, C. ZnO Nanorod Arrays for Photoelectrochemical Cells. *J Nanosci Nanotechnol* **2012**, *12* (5), 3984–3989. https://doi.org/10.1166/jnn.2012.6197.

(32) Mahala, C.; Sharma, M. D.; Basu, M. ZnO@CdS Heterostructures: An Efficient Photoanode for Photoelectrochemical Water Splitting. *New Journal of Chemistry* **2019**, *43* (18), 7001–7010. https://doi.org/10.1039/c9nj01373c.

(33) Diwate, K.; Rondia, S.; Mayabadi, A.; Rokade, A.; Waykar, R.; Borate, H.; Funde, A.; Shinde, M.; Rajedra Prasad, M. B.; Pathan, H.; Jadkar, S. Chemical Spray Pyrolysis Synthesis of Covellite Copper Sulphide (CuS) Thin Films for Economical Counter Electrode for DSSCs. *Journal of*

Materials Science: Materials in Electronics **2018**, *29* (6), 4940–4947. https://doi.org/10.1007/s10854-017-8453-6.

(34) Mora-Seró, I.; Fabregat-Santiago, F.; Denier, B.; Bisquert, J.; Tena-Zaera, R.; Elias, J.; Lévy-Clément, C. Determination of Carrier Density of ZnO Nanowires by Electrochemical Techniques. *Appl Phys Lett* **2006**, *89* (20), 1–4. https://doi.org/10.1063/1.2390667.

(35) Fabregat-Santiago, F.; Garcia-Belmonte, G.; Bisquert, J.; Bogdanoff, P.; Zaban, A. Mott-Schottky Analysis of Nanoporous Semiconductor Electrodes in Dielectric State Deposited on SnO[Sub 2](F) Conducting Substrates. *J Electrochem Soc* **2003**, *150* (6), E293. https://doi.org/10.1149/1.1568741.

(36) Pandit, B.; Rondiya, S. R.; Cross, R. W.; Dzade, N. Y.; Sankapal, B. R. Vanadium Telluride Nanoparticles on MWCNTs Prepared by Successive Ionic Layer Adsorption and Reaction for Solid-State Supercapacitor. *Chemical Engineering Journal* **2022**, *429*, 132505. https://doi.org/10.1016/j.cej.2021.132505.

(37) Joubert, D. From Ultrasoft Pseudopotentials to the Projector Augmented-Wave Method. *Phys Rev B Condens Matter Mater Phys* **1999**, *59* (3), 1758–1775. https://doi.org/10.1103/PhysRevB.59.1758.

(38) Kresse, G.; Furthmüller, J. Efficient Iterative Schemes for Ab Initio Total-Energy Calculations Using a Plane-Wave Basis Set. *Phys Rev B Condens Matter Mater Phys* **1996**, *54* (16), 11169–11186. https://doi.org/10.1103/PhysRevB.54.11169.

(39) Kresse, G.; Furthmüller, J. Efficiency of Ab-Initio Total Energy Calculations for Metals and Semiconductors Using a Plane-Wave Basis Set. *Comput Mater Sci* **1996**, *6* (1), 15–50. https://doi.org/10.1016/0927-0256(96)00008-0.

(40) Adamo, C.; Barone, V. Toward Reliable Density Functional Methods without Adjustable Parameters: The PBE0 Model. *Journal of Chemical Physics* **1999**, *110* (13), 6158–6170. https://doi.org/10.1063/1.478522.

(41) Ernzerhof, M.; Scuseria, G. E. Assessment of the Perdew-Burke-Ernzerhof Exchange-Correlation Functional. *J Chem Phys* **1999**, *110* (11), 5029–5036.

(42) Monkhorst, H. J.; Pack, J. D. Special Points for Brillouin-Zone Integrations. *Phys Rev B* **1976**, *13* (12), 5188–5192. https://doi.org/10.1103/PhysRevB.13.5188.

(43) Togo, A.; Tanaka, I. *Spglib: A Software Library for Crystal Symmetry Search*; 2018. http://arxiv.org/abs/1808.01590.

(44) Hinuma, Y.; Pizzi, G.; Kumagai, Y.; Oba, F.; Tanaka, I. Band Structure Diagram Paths Based on Crystallography. *Comput Mater Sci* **2017**, *128*, 140–184. https://doi.org/10.1016/j.commatsci.2016.10.015.

(45) M Ganose, A.; J Jackson, A.; O Scanlon, D. Sumo: Command-Line Tools for Plotting and Analysis of Periodic Ab Initio Calculations. *J Open Source Softw* **2018**, *3* (28), 717. https://doi.org/10.21105/joss.00717.

(46) Momma, K.; Izumi, F. VESTA 3 for Three-Dimensional Visualization of Crystal, Volumetric and Morphology Data. *J Appl Crystallogr* **2011**, *44* (6), 1272–1276. https://doi.org/10.1107/S0021889811038970.

(47) Mostofi, A. A.; Yates, J. R.; Pizzi, G.; Lee, Y. S.; Souza, I.; Vanderbilt, D.; Marzari, N. An Updated Version of Wannier90: A Tool for Obtaining Maximally-Localised Wannier Functions. *Comput Phys Commun* **2014**, *185* (8), 2309–2310. https://doi.org/10.1016/j.cpc.2014.05.003.

(48) Marzari, N.; Vanderbilt, D. Maximally Localized Generalized Wannier Functions for Composite Energy Bands. *Phys Rev B* **1997**, *56* (20), 12847. https://doi.org/10.1103/PhysRevB.65.035109.

(49) Marzari, N.; Mostofi, A. A.; Yates, J. R.; Souza, I.; Vanderbilt, D. Maximally Localized Wannier Functions: Theory and Applications. *Rev Mod Phys* **2012**, *84* (4), 1419–1475. https://doi.org/10.1103/RevModPhys.84.1419.

(50) Watson, G. W.; Kelsey, E. T.; de Leeuw, N. H.; Harris, D. J.; Parker, S. C. Atomistic Simulation of Dislocations, Surfaces and Interfaces in MgO. *Journal of the Chemical Society - Faraday Transactions* **1996**, *92* (3), 433–438. https://doi.org/10.1039/ft9969200433.

(51) Hinuma, Y.; Grüneis, A.; Kresse, G.; Oba, F. Band Alignment of Semiconductors from Density-Functional Theory and Many-Body Perturbation Theory. *Phys Rev B Condens Matter Mater Phys* **2014**, *90* (15), 155405. https://doi.org/10.1103/PhysRevB.90.155405.

(52) Hinuma, Y.; Oba, F.; Kumagai, Y.; Tanaka, I. Ionization Potentials of (112) and (11$\bar{2}$) Facet Surfaces of CuInSe2 and CuGaSe2. *Phys Rev B Condens Matter Mater Phys* **2012**, *86* (24), 245433. https://doi.org/10.1103/PhysRevB.86.245433.

(53) Butler, K. T.; Buckeridge, J.; Catlow, C. R. A.; Walsh, A. Crystal Electron Binding Energy and Surface Work Function Control of Tin Dioxide. *Phys Rev B Condens Matter Mater Phys* **2014**, *89* (11), 115320. https://doi.org/10.1103/PhysRevB.89.115320.

(54) Yang, R. X.; Butler, K. T.; Walsh, A. Assessment of Hybrid Organic-Inorganic Antimony Sulfides for Earth-Abundant Photovoltaic Applications. *Journal of Physical Chemistry Letters* **2015**, *6* (24), 5009–5014. https://doi.org/10.1021/acs.jpclett.5b02555.

(55) Dovesi, R and Saunders, VR and Roetti, C and Orlando, R and Zicovich-Wilson, CM and Pascale, F and Civalleri, B and Doll, K and Harrison, NM and Bush, I. and others. *CRYSTAL17 User's Manual*; Gruppo di Chimica Teorica, Dipartimento di Chimica, 2017.

(56) Linnera, J.; Sansone, G.; Maschio, L.; Karttunen, A. J. Thermoelectric Properties of P-Type Cu2O, CuO, and NiO from Hybrid Density Functional Theory. *Journal of Physical Chemistry C* **2018**, *122* (27), 15180–15189. https://doi.org/10.1021/acs.jpcc.8b04281.

(57) Linnera, J.; Karttunen, A. J. Ab Initio Study of the Lattice Thermal Conductivity of Cu 2 O Using the Generalized Gradient Approximation and Hybrid Density Functional Methods. *Phys Rev B* **2017**, *96* (1), 014304. https://doi.org/10.1103/PhysRevB.96.014304.

(58) Zicovich-Wilson, C. M.; Pascale, F.; Roetti, C.; Saunders, V. R.; Orlando, R.; Dovesi, R. Calculation of the Vibration Frequencies of α-Quartz: The Effect of Hamiltonian and Basis Set. *J Comput Chem* **2004**, *25* (15), 1873–1881. https://doi.org/10.1002/jcc.20120.

(59) Karttunen, A. J.; Tynell, T.; Karppinen, M. Atomic-Level Structural and Electronic Properties of Hybrid Inorganic-Organic ZnO:Hydroquinone Superlattices Fabricated by ALD/MLD. J. Phys. Chem. C 2015, 119 (23), 13105−13114.

(60) Linnera, J.; Sansone, G.; Maschio, L.; Karttunen, A. J. Thermoelectric Properties of P-Type Cu2O, CuO, and NiO from Hybrid Density Functional Theory. Journal of Physical Chemistry C 2018, 122 (27), 15180–15189. https://doi.org/10.1021/acs.jpcc.8b04281.

(61) Linnera, J.; Karttunen, A. J. Ab Initio Study of the Lattice Thermal Conductivity of Cu2 O Using the Generalized Gradient Approximation and Hybrid Density Functional Methods. Phys Rev B 2017, 96 (1), 014304. https://doi.org/10.1103/PhysRevB.96.014304.

(62) Peralta, J. E.; Heyd, J.; Scuseria, G. E.; Martin, R. L. Spin-Orbit Splittings and Energy Band Gaps Calculated with the Heyd-Scuseria-Ernzerhof Screened Hybrid Functional. *Phys Rev B Condens Matter Mater Phys* **2006**, *74* (7), 174101. https://doi.org/10.1103/PhysRevB.74.073101.

(63) Tian, Z. R.; Voigt, J. A.; Liu, J.; Mckenzie, B.; Mcdermott, M. J.; Rodriguez, M. A.; Konishi, H.; Xu, H. Complex and Oriented ZnO Nanostructures. *Nat Mater* **2003**, *2* (12), 821–826. https://doi.org/10.1038/nmat1014.

(64) Mo, M.; Yu, J. C.; Zhang, L.; Li, S. K. A. Self-Assembly of ZnO Nanorods and Nanosheets into Hollow Microhemispheres and Microspheres. *Advanced Materials* **2005**, *17* (6), 756–760. https://doi.org/10.1002/adma.200401477.

(65) Hu, C.; Zeng, X.; Cui, J.; Chen, H.; Lu, J. Size Effects of Raman and Photoluminescence Spectra of CdS Nanobelts. *Journal of Physical Chemistry C* **2013**, *117* (40), 20998–21005. https://doi.org/10.1021/jp407272u.

(66) Shen, Q.; Zhao, X.; Zhou, S.; Hou, W.; Zhu, J. J. ZnO/CdS Hierarchical Nanospheres for Photoelectrochemical Sensing of Cu2+. *Journal of Physical Chemistry C* **2011**, *115* (36), 17958–17964. https://doi.org/10.1021/jp203868t.

(67) Fan, D.; Thomas, P. J.; O'Brien, P. Deposition of CdS and ZnS Thin Films at the Water/Toluene Interface. *J Mater Chem* **2007**, *17* (14), 1381–1386. https://doi.org/10.1039/b616004b.

(68) Kaidashev, E. M.; Lorenz, M.; Von Wenckstern, H.; Rahm, A.; Semmelhack, H. C.; Han, K. H.; Benndorf, G.; Bundesmann, C.; Hochmuth, H.; Grundmann, M. High Electron Mobility of Epitaxial ZnO Thin Films on C-Plane Sapphire Grown by Multistep Pulsed-Laser Deposition. *Appl Phys Lett* **2003**, *82* (22), 3901–3903. https://doi.org/10.1063/1.1578694.

(69) Kazmerski, L. L.; Berry, W. B.; Allen, C. W. Role of Defects in Determining the Electrical Properties of CdS Thin Films. I. Grain Boundaries and Surfaces. *J Appl Phys* **1972**, *43* (8), 3515–3521. https://doi.org/10.1063/1.1661746.

(70) Chen, Z.; Jaramillo, T. F.; Deutsch, T. G.; Kleiman-Shwarsctein, A.; Forman, A. J.; Gaillard, N.; Garland, R.; Takanabe, K.; Heske, C.; Sunkara, M.; McFarland, E. W.; Domen, K.; Milled, E. L.; Dinh, H. N. Accelerating Materials Development for Photoelectrochemical Hydrogen Production: Standards for Methods, Definitions, and Reporting Protocols. *J Mater Res* **2010**, *25* (1), 3–16. https://doi.org/10.1557/jmr.2010.0020.

(71) Guo, S.-T.; Tang, Z.-Y.; Du, Y.-W.; Liu, T.; Ouyang, T.; Liu, Z.-Q. Chlorine Anion Stabilized Cu2O/ZnO Photocathode for Selective CO2 Reduction to CH4. *Appl Catal B* **2023**, *321*, 122035. https://doi.org/10.1016/j.apcatb.2022.122035.

(72) Han, J.; Liu, Z.; Guo, K.; Zhang, X.; Hong, T.; Wang, B. AgSbS2 Modified ZnO Nanotube Arrays for Photoelectrochemical Water Splitting. *Appl Catal B* **2015**, *179*, 61–68. https://doi.org/10.1016/j.apcatb.2015.05.008.

(73) Wu, W. Q.; Xu, Y. F.; Rao, H. S.; Su, C. Y.; Kuang, D. Bin. Multistack Integration of Three-Dimensional Hyperbranched Anatase Titania Architectures for High-Efficiency Dye-Sensitized Solar Cells. *J Am Chem Soc* **2014**, *136* (17), 6437–6445. https://doi.org/10.1021/ja5015635.

(74) He, S.; Yan, C.; Chen, X.-Z.; Wang, Z.; Ouyang, T.; Guo, M.-L.; Liu, Z.-Q. Construction of Core-Shell Heterojunction Regulating α-Fe2O3 Layer on CeO2 Nanotube Arrays Enables Highly Efficient Z-Scheme Photoelectrocatalysis. *Appl Catal B* **2020**, *276*, 119138. https://doi.org/10.1016/j.apcatb.2020.119138.

(75) Malashchonak, M. V.; Mazanik, A. V.; Korolik, O. V.; Streltsov, E. A.; Kulak, A. I. Influence of Wide Band Gap Oxide Substrates on the Photoelectrochemical Properties and Structural Disorder of CdS Nanoparticles Grown by the Successive Ionic Layer Adsorption and Reaction (SILAR) Method. *Beilstein Journal of Nanotechnology* **2015**, *6* (1), 2252–2262. https://doi.org/10.3762/bjnano.6.231.

(76) Mayabadi, A.; Pawbake, A.; Rondiya, S.; Rokade, A.; Waykar, R.; Jadhavar, A.; Date, A.; Sharma, V.; Prasad, M.; Pathan, H.; Jadkar, S. Synthesis, Characterization, and Photovoltaic Properties of

TiO2/CdTe Core-Shell Heterostructure for Semiconductor-Sensitized Solar Cells (SSSCs). *Journal of Solid State Electrochemistry* **2017**, *21* (9), 2665–2676. https://doi.org/10.1007/s10008-016-3473-3.

(77) Chou, T. P.; Zhang, Q.; Fryxell, G. E.; Cao, G. Hierarchically Structured ZnO Film for Dye-Sensitized Solar Cells with Enhanced Energy Conversion Efficiency. *Advanced Materials* **2007**, *19* (18), 2588–2592. https://doi.org/10.1002/adma.200602927.

(78) Gao, X. F.; Li, H. B.; Sun, W. T.; Chen, Q.; Tang, F. Q.; Peng, L. M. CdTe Quantum Dots-Sensitized TiO2 Nanotube Array Photoelectrodes. *Journal of Physical Chemistry C* **2009**, *113* (18), 7531–7535. https://doi.org/10.1021/jp810727n.

(79) Han, J.; Liu, Z.; Guo, K.; Zhang, X.; Hong, T.; Wang, B. AgSbS2Modified ZnO Nanotube Arrays for Photoelectrochemical Water Splitting. Appl. Catal., B 2015, 179, 61−68.

(80) Wu, W. Q.; Xu, Y. F.; Rao, H. S.; Su, C. Y.; Kuang, D. B. Multistack Integration of Three-Dimensional Hyperbranched Anatase Titania Architectures for High-Efficiency Dye-Sensitized Solar Cells. J. Am. Chem. Soc. 2014, 136 (17), 6437−6445.

(81) Liberatore, M.; Decker, F.; Burtone, L.; Zardetto, V.; Brown, T. M.; Reale, A.; Di Carlo, A. Using EIS for Diagnosis of Dye-Sensitized Solar Cells Performance. *J Appl Electrochem* **2009**, *39* (11), 2291–2295. https://doi.org/10.1007/s10800-009-9806-5.

(82) Zehra, S.; Aslam, R.; Mobin, M. Electrochemical Impedance Spectroscopy: A Useful Tool for Monitoring the Performance of Corrosion Inhibitors. In *Recent Developments in Analytical Techniques for Corrosion Research*; Springer International Publishing: Cham, 2022; pp 91–117. https://doi.org/10.1007/978-3-030-89101-5_5.

(83) Leuaa, P.; Priyadarshani, D.; Choudhury, D.; Maurya, R.; Neergat, M. Resolving Charge-Transfer and Mass-Transfer Processes of VO2+/VO2+redox Species across the Electrode/Electrolyte Interface Using Electrochemical Impedance Spectroscopy for Vanadium Redox Flow Battery. *RSC Adv* **2020**, *10* (51), 30887–30895. https://doi.org/10.1039/d0ra05224h.

(84) Klotz, D.; Ellis, D. S.; Dotan, H.; Rothschild, A. Empirical: In Operando Analysis of the Charge Carrier Dynamics in Hematite Photoanodes by PEIS, IMPS and IMVS. *Physical Chemistry Chemical Physics* **2016**, *18* (34), 23438–23457. https://doi.org/10.1039/c6cp04683e.

(85) Zhang, K.; Guo, L. Metal Sulphide Semiconductors for Photocatalytic Hydrogen Production. *Catal Sci Technol* **2013**, *3* (7), 1672–1690. https://doi.org/10.1039/c3cy00018d.

(86) Kaur, D.; Bharti, A.; Sharma, T.; Madhu, C. Dielectric Properties of ZnO-Based Nanocomposites and Their Potential Applications. *Int J Opt* **2021**, *2021*, 1–20. https://doi.org/10.1155/2021/9950202.

(87) Unal, F.; Aktas, S.; Kurt, M. S.; Kabaer, M. Fabrication of Organic Interfacial Layered Ag/Cd-Doped ZnO Hybrid Optoelectronic Device: The Effect of Light on Its Electrical Parameters. *J Mater Res* **2023**, *38* (8), 2302–2314. https://doi.org/10.1557/s43578-023-00969-z.

(88) Cooper, M. J.; Panke, D. Anharmonic Thermal Vibrations in Mg2Si. *Acta Crystallographica Section A* **1970**, *26* (2), 292–293. https://doi.org/10.1107/S0567739470000682.

(89) Moormann, H.; Kohl, D.; Heiland, G. Variations of Work Function and Surface Conductivity on Clean Cleaved Zinc Oxide Surfaces by Annealing and by Hydrogen Adsorption. *Surf Sci* **1980**, *100* (2), 302–314. https://doi.org/10.1016/0039-6028(80)90374-X.

TOC GRAPHIC

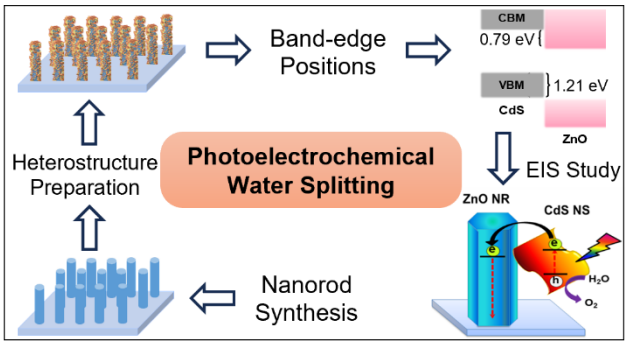
Band-edge
Positions
CBM
0.79 eV
VBM
1.21 eV
CdS
ZnO
Heterostructure
Preparation
Photoelectrochemical
Water Splitting
EIS Study
ZnO NR
CdS NS
e
h
H_2O
O_2
Nanorod
Synthesis